Available online at www.sciencedirect.com
SCIENCE DIRECT
Journal of Computational Physics 216 (2006) 589–615
JOURNAL OF COMPUTATIONAL PHYSICS
www.elsevier.com/locate/jcp

An anelastic allspeed projection method for gravitationally stratified flows ☆

Caroline Gatti-Bono *, Phillip Colella

Lawrence Berkeley National Laboratory, Berkeley, CA, United States

Received 19 April 2005; received in revised form 21 December 2005; accepted 23 December 2005
Available online 21 February 2006

Abstract

This paper looks at gravitationally stratified atmospheric flows at low Mach and Froude numbers and proposes a new algorithm to solve the compressible Euler equations, in which the asymptotic limits are recovered numerically and the boundary conditions for block-structured local refinement methods are well-posed.

The model is non-hydrostatic and the numerical algorithm uses a splitting to separate the fast acoustic dynamics from the slower anelastic dynamics. The acoustic waves are treated implicitly while the anelastic dynamics is treated semi-implicitly and an embedded-boundary method is used to represent orography. We present an example that verifies our asymptotic analysis and a set of results that compares very well with the classical gravity wave results presented by Durran.

Keywords: Non-hydrostatic atmospheric model; Embedded-boundary method; Projection method; Gravity waves

0. Introduction

Gravitationally stratified flows in a compressible medium at low Mach and Froude numbers arise in atmospheric fluid dynamics or in the modeling of stars. Traditionally, such flows have been simulated either by solving the fully compressible equations or by the use of hydrostatic or anelastic models [4,5,7,10–13,16,18,20–24,28,31,32]. Each of these formulations is desirable for particular properties in various asymptotic limits. Our goal is to obtain these various limits numerically from a discretization of the full compressible equations, depending on the scales being resolved. In addition, we seek a formulation for which the acoustic dynamics, the dynamics due to stiff gravity waves, and the advective dynamics, can be separated out and each treated with a suitable explicit or implicit method. Finally, we are looking for a formulation that admits well-posed general boundary-value problems. The latter property is essential for the development of block-structured local refinement methods, but, for example, does not hold for hydrostatic models [27].

☆ Supported at the Lawrence Berkeley National Laboratory by the US Department of Energy: Director, Office of Science, Office of Advanced Scientific Computing, Mathematical, Information, and Computing Sciences Division under Contract DE-AC03-76SF00098.
* Corresponding author. Tel.: +1 925 424 2084; fax: +1 925 422 6287.
E-mail addresses: cbono@llnl.gov (C. Gatti-Bono), pcolella@lbl.gov (P. Colella).

0021-9991/$ - see front matter
doi:10.1016/j.jcp.2005.12.017

In this paper, we describe a new algorithm for the compressible flow equations in a thin, gravitationally stratified layer that takes us part of the way in meeting these goals. It is based on an extension of the allspeed projection algorithm developed by Colella and Pao [9] to the case of an anelastic Hodge decomposition of the velocity field into solenoidal and potential components, along with a corresponding splitting of the pressure field. We further modify this splitting to correctly represent the dynamics of gravity waves for thin layers. This allows us to use an implicit method for treating the acoustic modes, combined with a semi-implicit method for the anelastic dynamics. We combine this method with appropriate spatial discretizations, including an embedded boundary treatment of orography. The resulting method has as a time step limitation the CFL condition for the fast gravity waves. Since the compressible flow equations have a well-posed boundary-value formulation, the overall method is well-posed. In addition, the individual PDEs that are solved in the various substeps have well-posed boundary-value formulations, thus making it a suitable starting point for an extension to locally refined meshes. Furthermore, since the splitting is of the full equations, there is a natural embedding of the thin-layer asymptotics into a more complete fundamental system of equations in multiscale calculations, in which the resolved horizontal scales become locally comparable to the vertical scales.

We test the method on two problems. The first comes from using thin-layer asymptotics and normal-mode analysis to derive the dynamics of fast gravity waves. We use the fully compressible algorithm described above to compute the propagation of these waves, and obtain results compatible with the asymptotic analysis. We also use the method to compute the test problems of Durran [10] for lee waves over a mountain, and obtain good agreement with the results in the literature. In the conclusions, we discuss possible approaches to eliminating the constraint on the time step due to the fast gravity waves.

1. Anelastic allspeed formulation

1.1. Equations

We consider a compressible inviscid fluid, described by the Euler equations

$$\frac{\partial \rho}{\partial t} + \operatorname{div}(\rho \mathbf{u}) = 0 \tag{1}$$

$$\frac{\partial \mathbf{u}}{\partial t} + \mathbf{u} \cdot \mathbf{grad}(\mathbf{u}) + \frac{1}{\rho}\mathbf{grad}(p) + g\mathbf{k} = 0 \tag{2}$$

$$\frac{\partial p}{\partial t} + \mathbf{u} \cdot \mathbf{grad}(p) + \rho c^2 \operatorname{div}(\mathbf{u}) = 0 \tag{3}$$

or, in perturbational form,

$$\frac{\partial \tilde{\rho}}{\partial t} + \operatorname{div}(\tilde{\rho}\mathbf{u}) + \operatorname{div}(\rho_0 \mathbf{u}) = 0 \tag{4}$$

$$\frac{\partial \mathbf{u}}{\partial t} + \mathbf{u} \cdot \mathbf{grad}(\mathbf{u}) + \frac{1}{\rho}\mathbf{grad}(\tilde{p}) + \frac{\tilde{\rho}}{\rho} g\mathbf{k} = 0 \tag{5}$$

$$\frac{\partial \tilde{p}}{\partial t} + \mathbf{u} \cdot \mathbf{grad}(\tilde{p}) + \rho c^2 \operatorname{div}(\mathbf{u}) - w\rho_0 g = 0 \tag{6}$$

Here, $\rho_0(z)$ is the hydrostatic density, $\tilde{\rho} = \rho - \rho_0$ is the perturbational density, $p_0(z)$ is the hydrostatic pressure defined as

$$\frac{\mathrm{d}p_0}{\mathrm{d}z} = -\rho_0 g \tag{7}$$

and $\tilde{p} = p - p_0$ is the perturbational pressure.

Eqs. (4)–(6) support acoustic waves and an explicit numerical discretization of these will require a time step dictated by the acoustic dynamics. However, since the acoustic waves have a negligible effect in atmospheric dynamics, using a small time step dictated by the vertical propagating acoustic waves, about 10 times smaller than the one dictated by the horizontally propagating gravity waves, is a huge performance loss. Therefore, we split the dynamics, separating the acoustic waves from the slower anelastic dynamics.

$$\mathbf{u} = \mathbf{u}_d + \mathbf{u}_p + \mathbf{u}_h \tag{8}$$

$$\mathrm{div}(\eta_0 \mathbf{u}_d) = 0 \tag{9}$$

$$\mathrm{div}(\eta_0 \mathbf{u}_h) = 0 \tag{10}$$

$$\mathbf{u}_p = \mathbf{grad}(\varphi) \tag{11}$$

$$\mathbf{u}_h = \mathbf{grad}(\upsilon) \tag{12}$$

where $\mathbf{u}$ is the total velocity, $\mathbf{u}_d$ is the anelastic velocity, $\mathbf{u}_p$ is the curl-free velocity and $\mathbf{u}_h$ is the harmonic velocity, and $\eta_0 = \eta_0(z)$ is a function to be determined later. The velocities must also satisfy the following relationships on Neumann boundaries:

$$\mathbf{u}_d \cdot \mathbf{n} = 0 \tag{13}$$

$$\mathbf{u}_p \cdot \mathbf{n} = 0 \tag{14}$$

$$\mathbf{u}_h \cdot \mathbf{n} = \mathbf{u} \cdot \mathbf{n} \tag{15}$$

The anelastic and curl-free velocities can also be obtained from the total velocity

$$\mathbf{u}_d = \mathbb{P}_0(\mathbf{u} - \mathbf{u}_h) \tag{16}$$

$$\mathbf{u}_p = \mathbb{Q}_0(\mathbf{u} - \mathbf{u}_h) \tag{17}$$

by using projection operators defined as follows:

$$\mathbb{Q}_0(\mathbf{w}) = \mathbf{grad}\left(\mathbb{L}_{\frac{1}{\eta_0}}\right)^{-1} \mathrm{div}(\eta_0 \mathbf{w}) \tag{18}$$

$$\mathbb{P}_0(\mathbf{w}) = (\mathbb{I} - \mathbb{Q}_0)(\mathbf{w}) \tag{19}$$

where $\mathbb{L}_{\frac{1}{\beta}}\varphi = \mathrm{div}(\beta\,\mathbf{grad}\,\varphi)$. The boundary conditions will be discussed later. Using the splitting, Eqs. (4)–(6) can be rewritten

$$\frac{\partial \tilde{\rho}}{\partial t} + \rho_0 w\left[\frac{1}{\rho_0}\frac{\mathrm{d}\rho_0}{\mathrm{d}z} - \frac{1}{\eta_0}\frac{\mathrm{d}\eta_0}{\mathrm{d}z}\right] + \mathrm{div}(\tilde{\rho}\mathbf{u}) + \frac{\rho_0}{\eta_0}\mathrm{div}(\eta_0 \mathbf{u}_p) = 0 \tag{20}$$

$$\frac{\partial \mathbf{u}_d}{\partial t} + \mathbf{A}_d\mathbf{u} + \frac{1}{\rho}\mathbf{grad}(\pi_I) + \frac{1}{\rho}\frac{\partial \pi_H}{\partial x}\mathbf{i} + \frac{1}{\rho}\mathbf{grad}(\psi) + \mathbb{P}_0\left[\frac{1}{\rho}\mathbf{grad}\delta + \mathbf{grad}\frac{|\mathbf{u}_p + \mathbf{u}_h|^2}{2}\right] = 0 \tag{21}$$

$$\frac{\partial \mathbf{u}_p}{\partial t} + \mathbb{Q}_0\left[\frac{1}{\rho}\mathbf{grad}\delta + \mathbf{grad}\frac{|\mathbf{u}_p + \mathbf{u}_h|^2}{2}\right] = 0 \tag{22}$$

$$\frac{\partial \delta}{\partial t} + \frac{\partial \pi_H}{\partial t} + \frac{\partial \pi_I}{\partial t} + \frac{\partial \psi}{\partial t} + \mathbf{u} \cdot \mathbf{grad}(\pi_I + \pi_H + \delta + \psi) + \frac{\rho c^2}{\eta_0}\mathrm{div}(\eta_0 \mathbf{u}_p) - w\left[\frac{\rho c^2}{\eta_0}\frac{\mathrm{d}\eta_0}{\mathrm{d}z} + \rho_0 g\right] = 0 \tag{23}$$

where the following quantities have been introduced:

- $\mathbf{i}$ is the unit vector in the horizontal direction.
- $\mathbf{A_d u}$ is the advective term defined as

$$\mathbf{A_d u} = (\mathbf{u} \cdot \mathbf{grad})\mathbf{u} - \mathbf{grad}\left(\frac{|\mathbf{u_p} + \mathbf{u_h}|^2}{2}\right) \tag{24}$$

- π_H and π_I are defined as

$$\frac{\partial \pi_H}{\partial z} = -\tilde{\rho} g \tag{25}$$

$$\frac{1}{\rho}(\mathbf{grad}\,\pi_I) = -\mathbb{Q}_\rho(\mathbf{A_d u}) \tag{26}$$

with

$$\mathbb{Q}_\rho \mathbf{w} = \frac{1}{\rho}\mathbf{grad}\left(\mathbb{L}_{\frac{\rho}{\eta_0}}\right)^{-1} \mathrm{div}\,\eta_0 \mathbf{w} \tag{27}$$

π_H is the perturbational hydrostatic pressure and π_I contains some of the effects of the incompressible motions.

- ψ is defined as

$$\frac{1}{\rho}\mathbf{grad}(\psi) = -\mathbb{Q}_\rho\left(\frac{1}{\rho}\frac{\partial \pi_H}{\partial x}\mathbf{i}\right) \tag{28}$$

ψ contains the vertical motions produced by horizontal gravity waves.

- δ is the "acoustic pressure"

$$\delta = p - p_0(z) - \pi - \psi \tag{29}$$

We choose η_0 to cancel the buoyancy term $\rho_0 g w$ in the pressure equation for the unperturbed reference state.

$$\frac{1}{\eta_0}\frac{\mathrm{d}\eta_0}{\mathrm{d}z} = -\frac{\rho_0 g}{\gamma p_0} = \frac{1}{\gamma p_0}\frac{\mathrm{d}p_0}{\mathrm{d}z}, \quad \eta_0(0) = \rho_0(0) \tag{30}$$

It is to be noted that η_0 comes out to be the isentropic density corresponding to the pressure distribution p_0. With this value of η_0, Eqs. (20)–(23) become

$$\frac{\partial \tilde{\rho}}{\partial t} - \frac{\rho_0 N^2}{g} w + \mathrm{div}(\tilde{\rho}\mathbf{u}) + \frac{\rho_0}{\eta_0}\mathrm{div}(\eta_0 \mathbf{u}_p) = 0 \tag{31}$$

$$\frac{\partial \mathbf{u}_d}{\partial t} + \mathbf{A}_d\mathbf{u} + \frac{1}{\rho}\mathbf{grad}(\pi_I) + \frac{1}{\rho}\frac{\partial \pi_H}{\partial x}\mathbf{i} + \frac{1}{\rho}\mathbf{grad}(\psi) + \mathbb{P}_0\left[\frac{1}{\rho}\mathbf{grad}\,\delta + \mathbf{grad}\frac{|\mathbf{u}_p + \mathbf{u}_h|^2}{2}\right] = 0 \tag{32}$$

$$\frac{\partial \mathbf{u}_p}{\partial t} + \mathbb{Q}_0\left[\frac{1}{\rho}\mathbf{grad}\,\delta + \mathbf{grad}\frac{|\mathbf{u}_p + \mathbf{u}_h|^2}{2}\right] = 0 \tag{33}$$

$$\frac{\partial \delta}{\partial t} + \frac{\partial \pi_H}{\partial t} + \frac{\partial \pi_I}{\partial t} + \frac{\partial \psi}{\partial t} + \mathbf{u}\cdot\mathbf{grad}(\pi_I + \pi_H + \delta + \psi) + \frac{\rho c^2}{\eta_0}\mathrm{div}(\eta_0 \mathbf{u}_p) + (\pi_I + \pi_H + \delta + \psi)\frac{\rho_0 g w}{p_0} = 0 \tag{34}$$

where N is the Brunt–Väisälä frequency defined by

$$\frac{N^2}{g} = \frac{1}{\eta_0}\frac{\mathrm{d}\eta_0}{\mathrm{d}z} - \frac{1}{\rho_0}\frac{\mathrm{d}\rho_0}{\mathrm{d}z} \tag{35}$$

1.2. Asymptotic analysis

We use asymptotic analysis techniques to demonstrate that the splitting of the dynamics described above leads to a separation of the acoustic and fast buoyant time scales. Our approach is similar to that used in [19], but with the goal of putting the equations in a form suitable for applying normal-mode analysis to derive the dynamics of fast gravity waves.

We start by linearizing Eqs. (31)–(34) around the state $\tilde{\rho} = 0$ and $(u, w) = 0$

$$\frac{\partial \tilde{\rho}}{\partial t} - \rho_0\frac{N^2}{g} w + \frac{\rho_0}{\eta_0}\mathrm{div}(\eta_0 \mathbf{u}_p) = 0 \tag{36}$$

$$\frac{\partial \mathbf{u}_d}{\partial t} + \frac{1}{\rho_0}\frac{\partial \pi_H}{\partial x}\mathbf{i} + \frac{1}{\rho_0}\mathbf{grad}(\psi) + \mathbb{P}_0\left[\frac{1}{\rho_0}\mathbf{grad}\,\delta\right] = 0 \tag{37}$$

$$\frac{\partial \mathbf{u}_p}{\partial t} + \mathbb{Q}_0\left[\frac{1}{\rho_0}\mathbf{grad}\,\delta\right] = 0 \tag{38}$$

$$\frac{\partial \delta}{\partial t} + \frac{\partial \pi_H}{\partial t} + \frac{\partial \psi}{\partial t} + \frac{\rho_0 c_0^2}{\eta_0}\mathrm{div}(\eta_0 \mathbf{u}_p) = 0 \tag{39}$$

If U is the horizontal velocity scale, $\bar{c}$ is the average speed of sound, Λ is the speed of a typical gravity wave, l_v is the vertical length scale, L is the horizontal length scale, $\overline{N}$ is the average Brunt–Väisälä and g is the gravity constant, we can introduce the following dimensionless variables:

$$\hat{x} = \frac{x}{L} \tag{40}$$

$$\varepsilon = \frac{l_v}{L} \tag{41}$$

$$\hat{z} = \frac{z}{\varepsilon L} \tag{42}$$

$$\Lambda = \sqrt{\varepsilon L g} = \varepsilon L \overline{N} \tag{43}$$

$$\hat{t} = \frac{\Lambda}{L} t \tag{44}$$

$$\hat{u} = \frac{u}{U} \tag{45}$$

$$\hat{w} = \frac{w}{W} \tag{46}$$

$$\hat{u_d} = \frac{u_d}{U_d} \tag{47}$$

$$\hat{w_d} = \frac{w_d}{W_d} \tag{48}$$

$$\hat{u_p} = \frac{u_p}{U_p} \tag{49}$$

$$\hat{w_p} = \frac{w_p}{W_p} \tag{50}$$

$$\mathscr{F}r = \frac{U}{\Lambda} \tag{51}$$

$$\mathscr{M} = \frac{U}{\bar{c}} \tag{52}$$

where $\mathscr{M}$ is the Mach number, ε is the aspect ratio and $\mathscr{F}r$ is the Froude number. Our choice of time scale reflects the fact that the fast gravity waves are of interest in this study.

For mesoscale atmospheric flows, we have the following relationships between the different parameters defined above:

$$\varepsilon \ll 1 \tag{53}$$

$$\mathscr{M} \sim \mathscr{F}r \ll 1 \tag{54}$$

$$W_d = \varepsilon U_d \tag{55}$$

Using Eq. (11), we obtain

$$W_p = \frac{U_p}{\varepsilon} \tag{56}$$

These parameters are used to estimate the magnitude of the different contributions to the pressure π_H, ψ and δ (π_I depends quadratically on $\mathbf{u}$ and is therefore negligible in the present analysis). Using Eqs. (36)–(38) along with the definitions of π_H and ψ, multiplying by η_0 and applying the divergence operator, we obtain

$$\frac{\bar{\rho}\Lambda U_p}{L^2}\left(\frac{\partial}{\partial\hat{x}}\left(\hat{\eta_0}\frac{\partial\hat{u}_p}{\partial\hat{t}}\right)+\frac{1}{\varepsilon^2}\frac{\partial}{\partial\hat{z}}\left(\hat{\eta_0}\frac{\partial\hat{w}_p}{\partial\hat{t}}\right)\right)+\frac{1}{L^2}\left(\frac{\partial}{\partial\hat{x}}\left(\frac{\hat{\eta}_0}{\hat{\rho}_0}\frac{\partial\delta}{\partial\hat{x}}\right)+\frac{1}{\varepsilon^2}\frac{\partial}{\partial\hat{z}}\left(\frac{\hat{\eta}_0}{\hat{\rho}_0}\frac{\partial\delta}{\partial\hat{z}}\right)\right)=0 \tag{57}$$

$$\frac{\partial}{\partial\hat{z}}\left(\frac{\partial\pi_H}{\partial\hat{t}}\right)=-\bar{\rho}\Lambda U\hat{\rho}_0\widehat{N}^2\hat{w}+\bar{\rho}\Lambda U_p\frac{\hat{\rho}_0}{\hat{\eta}_0}\left(\frac{\partial\hat{\eta}_0\hat{u}_p}{\partial\hat{x}}+\frac{1}{\varepsilon^2}\frac{\partial\hat{\eta}_0\hat{w}_p}{\partial\hat{z}}\right) \tag{58}$$

$$\frac{\bar{\rho}\Lambda U_d}{L^2}\left(\frac{\partial}{\partial\hat{x}}\left(\hat{\eta_0}\frac{\partial\hat{u}_d}{\partial\hat{t}}\right)+\frac{\partial}{\partial\hat{z}}\left(\hat{\eta_0}\frac{\partial\hat{w}_d}{\partial\hat{t}}\right)\right)+\frac{1}{L^2}\left(\frac{\hat{\eta_0}}{\hat{\rho_0}}\frac{\partial^2\pi_H}{\partial\hat{x}^2}+\frac{\hat{\eta_0}}{\hat{\rho_0}}\frac{\partial^2\psi}{\partial\hat{x}^2}+\frac{1}{\varepsilon^2}\frac{\partial}{\partial\hat{z}}\left(\frac{\hat{\eta_0}}{\hat{\rho_0}}\frac{\partial\psi}{\partial\hat{z}}\right)\right)=0 \tag{59}$$

$$\frac{1}{L^2}\frac{\partial}{\partial\hat{x}}\left(\frac{\hat{\eta}_0}{\hat{\rho}_0}\frac{\partial\psi}{\partial\hat{x}}\right)+\frac{1}{\varepsilon^2L^2}\frac{\partial}{\partial\hat{z}}\left(\frac{\hat{\eta}_0}{\hat{\rho}_0}\frac{\partial\psi}{\partial\hat{z}}\right)=-\frac{1}{L^2}\frac{\partial}{\partial\hat{x}}\left(\frac{\hat{\eta}_0}{\hat{\rho}_0}\frac{\partial\pi_H}{\partial\hat{x}}\right) \tag{60}$$

$$U\hat{u}=U_d\hat{u}_d+U_p\hat{u}_p \tag{61}$$

This gives us the following estimates of the magnitude for the velocities and the various pressure terms:

$$U_p = \mathrm{O}(\varepsilon^2 U_d) \tag{62}$$
$$U_d = \mathrm{O}(U) \tag{63}$$
$$\pi_H = \mathrm{O}(\bar{\rho} \Lambda U) \tag{64}$$
$$\delta, \psi = \mathrm{O}(\varepsilon^2 \bar{\rho} \Lambda U) \tag{65}$$

From this it follows that (39) reduces to

$$\frac{1}{\rho_0 c_0^2} \frac{\partial \pi_H}{\partial t} + \frac{1}{\eta_0} \mathrm{div}(\eta_0 \mathbf{u}_p) = \mathrm{O}\left(\varepsilon^2 \frac{U}{L}\right) \tag{66}$$

Each term in the left-hand side is individually $\mathrm{O}(\frac{U}{L})$. Note that we have used assumption (54) in the derivation of (66).

We note now that the velocities satisfy the following relationships:

$$u_d = \mathrm{O}(U) \tag{67}$$
$$u_p = \mathrm{O}(\varepsilon^2 U) \tag{68}$$
$$w_d = \mathrm{O}(\varepsilon U) \tag{69}$$
$$w_p = \mathrm{O}(\varepsilon U) \tag{70}$$

Therefore, w_d and w_p are of comparable magnitude and w_p must be included in the equations to account for the complete vertical dynamics. In the pseudo-incompressible approximation [11], the divergence-free constraint is applied to the total velocity

$$\mathrm{div}(\eta_0 \mathbf{u}) = 0 \tag{71}$$

which is equivalent to discarding the potential velocity $\mathbf{u}_p$, which leads to advective dynamics different from the present approach.

Also, we recover the classical assumption

$$W = \varepsilon U \tag{72}$$

i.e. that the horizontal and vertical advective time scales are comparable.

Eq. (66) is used to derive a system of hyperbolic equations (as shown in the Appendix)

$$\mathscr{L}_z \frac{\partial \pi_H}{\partial t} + \eta_0 \frac{\partial u_d}{\partial x} = \mathrm{O}(\varepsilon^2) \tag{73}$$
$$\frac{\partial u_d}{\partial t} + \frac{1}{\rho_0} \frac{\partial \pi_H}{\partial x} = \mathrm{O}(\varepsilon^2) \tag{74}$$

where

$$\mathscr{L}_z = -\frac{\partial}{\partial z}\left[\frac{\eta_0 g}{\rho_0 N^2}\left(\frac{1}{g}\frac{\partial}{\partial z} + \frac{1}{c_0^2}\right)\right] + \frac{\eta_0}{\rho_0 c_0^2} \tag{75}$$

The operator $\mathscr{L}_z$ can be rewritten in the form

$$\mathscr{L}_z = -\frac{\partial}{\partial z}\left[\frac{\eta_0 g}{\rho_0 N^2}\left(\frac{1}{g}\frac{\partial}{\partial z} + \frac{1}{c_0^2}\right)\right] + \frac{\eta_0}{\rho_0 c_0^2} = -\xi\left[\frac{\partial}{\partial z}\zeta\frac{\partial}{\partial z} + \chi\right] \tag{76}$$

with

$$\xi = \exp\left(-\int_0^z \frac{g}{c_0^2}\mathrm{d}z\right) \tag{77}$$
$$\zeta = \frac{\eta_0}{\rho_0 N^2}\exp\left(\int_0^z \frac{g}{c_0^2}\mathrm{d}z\right) \tag{78}$$
$$\chi = \frac{\eta_0}{\rho_0 c_0^2}\left[(\gamma - 1)\frac{g^2}{N^2 c_0^2} - 1\right]\exp\left(\int_0^z \frac{g}{c_0^2}\mathrm{d}z\right) \tag{79}$$

When χ is negative, the operator is positive definite and Eqs. (73) and (74) describe the motion of an infinite collection of horizontally propagating gravity waves, one for each eigenmode of the second-order self-adjoint operator $\mathscr{L}_z$. When χ is positive, the first few eigenvalues can become negative, as shown in Fig. 1, and this is a direct consequence of including the potential dynamics into the asymptotic analysis. We observe that this has a stabilizing effect as the modes with negative eigenvalues do not support gravity waves.

The asymptotic analysis in this section is similar to the normal mode analysis presented by Baer and Tribbia [2], Tribbia [34], Temperton and Williamson [33,35], but we use the full compressible PDEs instead of the discretized version of the hydrostatic equations. When the operator is positive definite, the eigenvalues λ^k are real and the (normalized) eigenvectors r^k form an orthonormal basis in L^2. The speeds of the gravity waves are then given by

$$c^k = \frac{1}{\sqrt{\lambda^k}} \tag{80}$$

and are shown in Fig. 2 for an example presented in the results section. This figure shows that the gravity waves for only a few modes travel faster than a typical fluid velocity for large-scale motions of 20 m/s (marked in a solid line on the graph). If these modes were isolated and treated implicitly, then we could use a CFL condition based only on the speed of the fluid, which could lead to a considerable gain in computational efficiency.

The results above are compatible with traditional analysis for incompressible or Boussinesq flows [30] where the following wave equation describes the vertical motion for small-amplitude perturbations:

$$\frac{\partial^2}{\partial t^2}\left(\frac{\partial^2 w_d}{\partial x^2} + \frac{\partial^2 w_d}{\partial z^2}\right) + N^2 \frac{\partial^2 w_d}{\partial x^2} = 0 \tag{81}$$

which yields the dispersion relationship

$$\omega^2 = \frac{k^2 N^2}{k^2 + m^2} \tag{82}$$

where k is the horizontal wave number and m is the vertical wave number. See for example [12] or [15]. We apply the same methodology to our set of Euler equations than the one used to derive (81) and we obtain

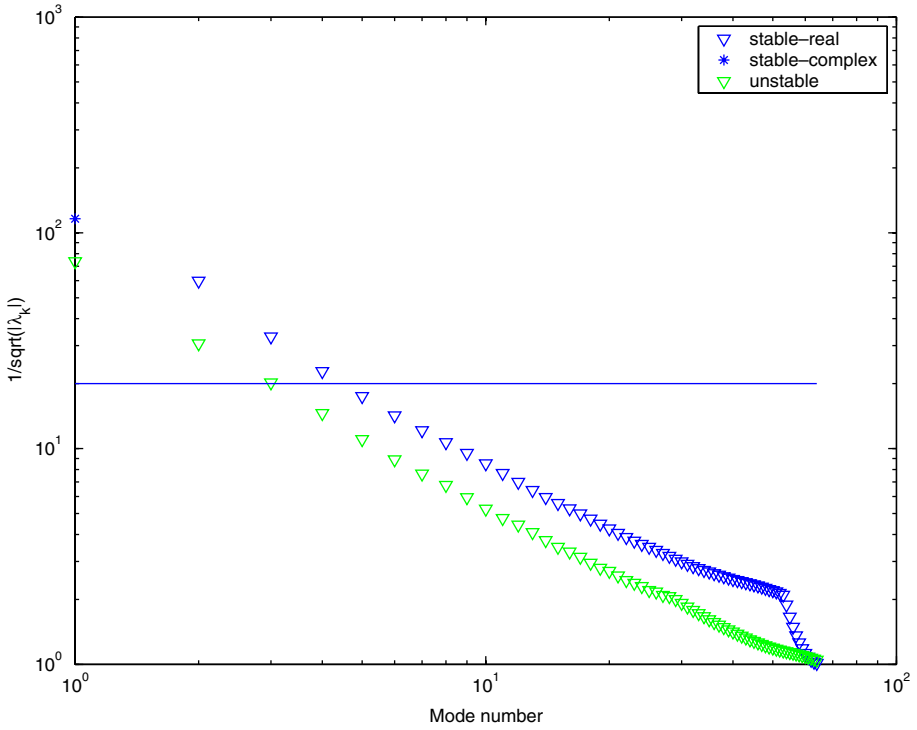

Fig. 1. "Speed" of gravity waves for the quarter-wavelength stable and unstable cases shown in the results section.

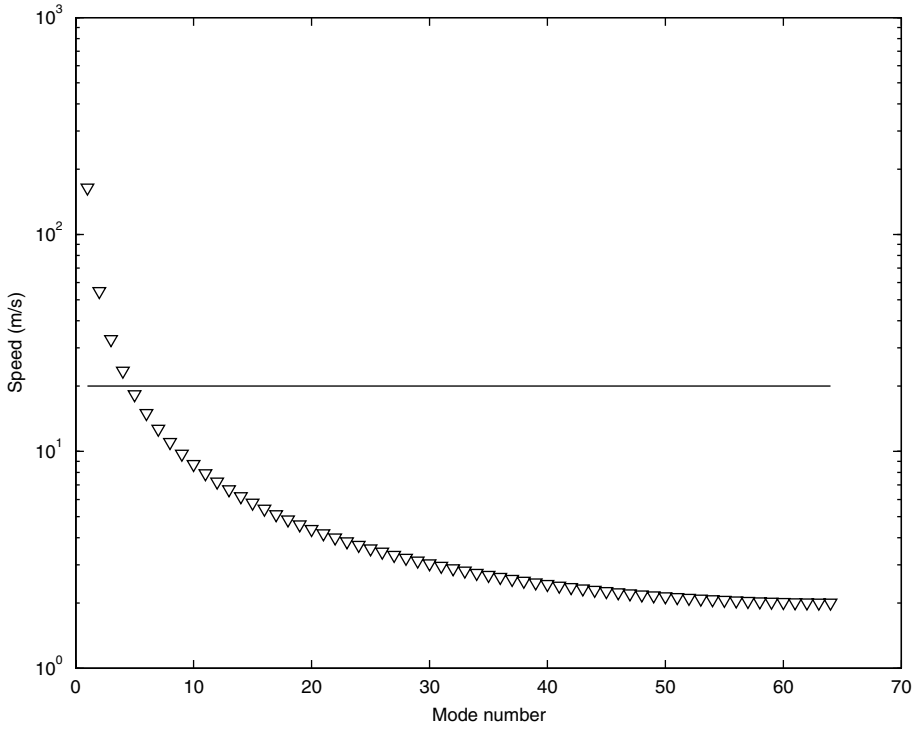

Fig. 2. Speed of gravity waves for the perturbational gravity-wave test problem of Section 4.

$$\frac{\partial^2}{\partial t^2}\left(\frac{\partial^2 w_d}{\partial x^2}+\frac{\partial}{\partial z}\frac{1}{\eta_0}\frac{\partial \eta_0 w_d}{\partial z}\right)-\frac{\partial^3}{\partial x^2 \partial z}\frac{1}{\rho_0}\frac{\partial \pi_H}{\partial t}=R_1 \tag{83}$$

with

$$R_1=-\frac{\partial^2}{\partial t \partial x}\left(\frac{\partial}{\partial z}\mathbb{P}_{o_x}\left(\frac{1}{\rho_0}\mathbf{grad}\,\delta\right)-\frac{\partial}{\partial x}\mathbb{P}_{o_z}\left(\frac{1}{\rho_0}\mathbf{grad}\,\delta\right)\right) \tag{84}$$

$$=-\frac{1}{\rho_0^2}\frac{\partial \rho_0}{\partial z}\frac{\partial^3 \delta}{\partial x^2 \partial t} \tag{85}$$

Using Eq. (73), we obtain

$$\frac{\partial^2}{\partial t^2}\left(\frac{\partial^2 w_d}{\partial x^2}+\frac{\partial}{\partial z}\frac{1}{\eta_0}\frac{\partial \eta_0 w_d}{\partial z}\right)-\frac{\partial^2}{\partial x^2}\left(\frac{\partial}{\partial z}\frac{1}{\rho_0}\mathscr{L}_z^{-1}\frac{\partial \eta_0 w_d}{\partial z}\right)=R_2 \tag{86}$$

where

$$R_2=R_1+\frac{\partial^3}{\partial x^2 \partial z}\frac{1}{\rho_0}\mathscr{L}_z^{-1}\left(-\frac{\partial}{\partial z}\left[\frac{\eta_0 g}{\rho_0 c_0^2 N^2}\frac{\partial \pi_H}{\partial t}+\frac{g}{N^2}\mathrm{div}(\eta_0 \mathbf{u}_p)\right]+\mathrm{div}(\eta_0 \mathbf{u}_p)+\frac{\eta_0}{\rho_0 c_0^2}\frac{\partial \pi_H}{\partial t}-\frac{\partial \eta_0 u_p}{\partial x}\right) \tag{87}$$

Now, if we consider the flow to be incompressible, we have

$$\rho_0=\eta_0 \tag{88}$$

$$\mathscr{L}_z=-\frac{\partial}{\partial z}\left(\frac{1}{N^2}\frac{\partial}{\partial z}\right) \tag{89}$$

$$\delta=0 \tag{90}$$

$$\mathbf{u}_p=0 \tag{91}$$

$$c_0\to\infty \tag{92}$$

and (86) becomes

$$\frac{\partial^2}{\partial t^2}\left(\frac{\partial^2 w_d}{\partial x^2}+\frac{\partial^2 w_d}{\partial z^2}\right)+N^2\frac{\partial^2 w_d}{\partial x^2}=0 \tag{93}$$

Therefore, we recover (81) from (86) when we use the same incompressibility hypothesis. It can also be noted that the parameter χ is zero when the flow is incompressible and as a result, the operator $\mathscr{L}_z$ is always positive definite, i.e. the eigenvalues are always real and positive.

The two main advantages of the normal mode analysis are that it is global and that it detects the stabilizing effects of compressibility for the long-wavelength normal modes.

2. Time discretization

In this section, we will introduce the quantities that are solved for and we will present only the time discretization that is used to advance the solution. We made the choice to dissociate time and spatial discretizations for clarity purposes. The time discretization of Eqs. (31)–(34) gives the blueprint of the numerical algorithm that should not be overshadowed by the technicalities of spatial discretizations and centerings, which can be found in the subsequent Section 3.

2.1. Variables and time discretization

Time is discretized using Δt. The variables that we solve for are the total velocity $\mathbf{u}=(u, w)$, the anelastic velocity $\mathbf{u}_d=(u_d, w_d)$, the curl-free velocity $\mathbf{u}_p=(u_p, w_p)$, the total pressure p, the acoustic pressure δ, the auxiliary pressures ψ, π_H and π_I, the density ρ, and the perturbational density $\tilde{\rho}$.

2.2. Time discretization of Eqs. (31)–(34)

The system (31)–(34) is discretized in time using a combination of explicit or implicit schemes. First, a few quantities are partially advanced, considering only the advective dynamics, so that the auxiliary pressure π_I can be advanced to half time step in order to compute the acoustic pressure. Then, the curl-free velocity is advanced and the quantities that were partially or temporarily advanced are corrected.

- First, the anelastic velocity is partially advanced in time using only the advection terms in Eq. (32)

$$\mathbf{u}_d^*=\mathbf{u}_d^n-\Delta t\left((\mathbf{A_d u})^{n+\frac{1}{2}}\right) \tag{94}$$

- Then, we use Eq. (31) to temporarily advance the density variables ρ and $\tilde{\rho}$

$$\tilde{\rho}^{*,n+1}=\tilde{\rho}^n+\Delta t\left(\frac{\partial\tilde{\rho}}{\partial t}\right)^{n+\frac{1}{2}} \tag{95}$$

$$\rho^{*,n+1}=\tilde{\rho}^{*,n+1}+\rho_0 \tag{96}$$

$$\rho^{n+\frac{1}{2}}=\frac{\rho^{*,n+1}+\rho^n}{2} \tag{97}$$

- Eq. (25) is used to temporarily advance π_H

$$\pi_H^{*,n+1}=\int_z^L \tilde{\rho}^{*,n+1} g\,\mathrm{d}\check{z}\quad(\pi_H(L)=0) \tag{98}$$

Here, L is the vertical upper bound of the domain.

- Using Eq. (26), we solve for $\pi_I^{n+\frac{1}{2}}$,

$$\frac{1}{\rho^{n+\frac{1}{2}}}\mathbf{grad}\left(\pi_I^{n+\frac{1}{2}}\right)=-\mathbb{Q}_{\rho^{n+\frac{1}{2}}}\left(\mathbf{A_d u}^{n+\frac{1}{2}}\right) \tag{99}$$

- Using Eq. (28), we solve for ψ^{n+1},

$$\mathbb{L}_{\frac{\rho^{*,n+1}}{\eta_0}}\left(\psi^{*,n+1}\right) = -\mathrm{div}\left(\frac{\eta_0}{\rho^{*,n+1}}\frac{\partial \pi_H^{*,n+1}}{\partial x}\mathbf{i}\right) \tag{100}$$

- Combining Eqs. (33) and (34), we implicitly advance the acoustic pressure

$$\begin{aligned}\mathbb{H}\delta^{n+1} &\equiv \left(\mathbb{I} - \Delta t^2 \frac{\gamma p^n}{\eta_0}\mathbb{L}_{\frac{\rho^{n+\frac{1}{2}}}{\eta_0}}\right)\delta^{n+1} \\ &= \delta^n - \Delta t\left[\frac{\gamma p^n}{\eta_0}\left\{\mathrm{div}\left(\eta_0 \mathbf{u}_p^n\right) - \Delta t\,\mathrm{div}\,\eta_0 \mathbf{grad}\left(\frac{\left|\mathbf{u}_p^n + \mathbf{u}_h\right|^2}{2}\right)\right\} + \mathbf{u}^{n+\frac{1}{2}}\cdot(\mathbf{grad}(\delta^n + \pi^n + \psi^n))\right. \\ &\quad \left. - w^{n+\frac{1}{2}}\left[\frac{\rho^n c^{n2}}{\eta_0}\frac{\mathrm{d}\eta_0}{\mathrm{d}z} + \rho_0 g\right]\right] - \left(\pi_I^{n+\frac{1}{2}} + \pi_H^{*,n+1} + \psi^{*,n+1} - \pi_I^{n-\frac{1}{2}} - \pi_H^n - \psi^n\right)\end{aligned} \tag{101}$$

where

$$w^{n+\frac{1}{2}} = w_d^{n+\frac{1}{2}} + w_p^n + w_h \tag{102}$$

- Then, we advance the curl-free velocity using Eq. (33)

$$u_p^{n+1} = u_p^n - \Delta t \mathbb{Q}_0\left(\mathbf{grad}\left(\frac{\left|\mathbf{u}_p^n + \mathbf{u}_h\right|^2}{2}\right) + \left(\frac{1}{\rho^n}\left(\mathbf{grad}\,\delta^{n+1}\right)\right)\right) \tag{103}$$

- The perturbational density is advanced using Eq. (31)

$$\tilde{\rho}^{n+1} = \tilde{\rho}^n - \Delta t\frac{\rho_0 N^2}{g}w^{n+\frac{1}{2}} - \Delta t\frac{\rho_0}{\eta_0}\mathrm{div}\left(\eta_0 \mathbf{u}_p^{n+1}\right) - \Delta t\,\mathrm{div}(\tilde{\rho}\mathbf{u})^{n+\frac{1}{2}} \tag{104}$$

- π_H is updated

$$\pi_H^{n+1} = \int_z^L \tilde{\rho}^{n+1} g\,\mathrm{d}\check{z} \quad (\pi_H(L) = 0) \tag{105}$$

- ψ is updated

$$\mathbb{L}_{\frac{\rho^{n+1}}{\eta_0}}(\psi^{n+1}) = -\mathrm{div}\left(\frac{\eta_0}{\rho^{n+1}}\frac{\partial \pi_H^{n+1}}{\partial x}\mathbf{i}\right) \tag{106}$$

- We finish advancing the divergence-free velocity

$$u_d^{n+1} = u_d^* - \Delta t\left(\frac{1}{\rho^{n+\frac{1}{2}}}\left(\mathbf{grad}\,\pi_I^{n+\frac{1}{2}}\right) + \frac{1}{\rho^{n+1}}\left(\mathbf{grad}\,\psi^{n+1}\right) + \frac{1}{\rho^{n+1}}\frac{\partial \pi_H^{n+1}}{\partial x}\mathbf{i} + \mathbb{P}^0\left(\frac{1}{\rho^n}\left(\mathbf{grad}\,\delta^{n+1}\right) + \mathbf{grad}\left(\frac{\left|\mathbf{u}_p^n + \mathbf{u}_h\right|^2}{2}\right)\right)\right) \tag{107}$$

2.3. Boundary conditions

2.3.1. Inflow

At an inflow boundary, the velocity field in an inviscid model must satisfy

$$\mathbf{u}\cdot\mathbf{n} = u_n \tag{108}$$

Because the splitting satisfies Eqs. (13)–(15), we have

$$\mathbf{u}_d \cdot \mathbf{n} = 0 \tag{109}$$

$$\mathbf{u}_p \cdot \mathbf{n} = 0 \tag{110}$$

$$\mathbf{u}_h \cdot \mathbf{n} = u_n \tag{111}$$

The density is held constant at inflow

$$\rho = \rho_0 \tag{112}$$

$$\tilde{\rho} = 0 \tag{113}$$

where ρ_0 is the hydrostatic density distribution.

Now, we look at the more complicated boundary conditions for the projection and Helmholtz operators of Eqs. (99)–(103). At the boundary, Eq. (99) becomes

$$\frac{1}{\rho^{n+\frac{1}{2}}} \frac{\partial \pi_I^{n+\frac{1}{2}}}{\partial n} = -\mathbf{n} \cdot \mathbb{Q}_{\rho^{n+\frac{1}{2}}}\left(\mathbf{A_d u}^{n+\frac{1}{2}}\right) \tag{114}$$

By definition of the splitting, the anelastic component must be parallel to the boundary near the boundary, as seen in Eqs. (13)–(15), and we obtain

$$\mathbf{n} \cdot \mathbb{P}_{\rho^{n+\frac{1}{2}}}\left(\mathbf{A_d u}^{n+\frac{1}{2}}\right) = 0 \tag{115}$$

and therefore

$$\frac{1}{\rho^{n+\frac{1}{2}}} \frac{\partial \pi_I^{n+\frac{1}{2}}}{\partial n} = -\mathbf{n} \cdot \left(\mathbf{A_d u}^{n+\frac{1}{2}}\right) \tag{116}$$

Similarly, after taking the dot product of Eq. (103) with the normal and using condition (110), we obtain

$$\mathbf{n} \cdot \left(\mathbf{grad}\left(\frac{\left|\mathbf{u}_p^n + \mathbf{u}_h\right|^2}{2} \right) + \left(\frac{1}{\rho^n} \left(\mathbf{grad}\, \delta^{n+1} \right) \right) \right) = 0 \tag{117}$$

and the outflow boundary condition for the Helmholtz equation (101) becomes

$$\frac{1}{\rho^n} \frac{\partial \delta^{n+1}}{\partial n} = \mathbf{grad}\left(\frac{\left|\mathbf{u}_p^n + \mathbf{u}_h\right|^2}{2} \right) \cdot \mathbf{n} \tag{118}$$

2.3.2. Outflow

On the outflow boundary, the pressure is imposed

$$p = p_0 \tag{119}$$

where p_0 is the hydrostatic pressure, and this implies

$$\delta = 0 \tag{120}$$

$$\pi_I = 0 \tag{121}$$

3. Spatial discretization

3.1. Discretizing Eqs. (31)–(34) on a regular grid

An anisotropic rectangular grid with spacing Δx and Δz is applied to the computational domain as shown in Fig. 4(a). We seek the solution to the system of Eqs. (31)–(34) either at cell centers (i, j) or at cells faces $(i+\frac{1}{2}, j)$ or $(i, j+\frac{1}{2})$, where $i = 1 \ldots N$ with N the number of cells in the horizontal direction and $j = 1 \ldots M$ with

Table 1
Spatial and time centering of main variables

	Cell-centered	Face-centered	$t^n = n\Delta t$	$t^{n+\frac{1}{2}} = \left(n+\frac{1}{2}\right)\Delta t$
(u, w)	√		√	
(u_d, w_d)	√		√	
(u_d, w_d)		√		√
(u_p, w_p)		√	√	
(u_h, w_h)		√	N/A	N/A
p	√		√	
δ	√		√	
π	√			√
π_H		√	√	
π_I	√			√
ρ	√		√	
$\tilde{\rho}$	√		√	

M the number of cells in the vertical direction. Table 1 gives the spatial and time centering of the main variables.

In this section, to simplify the exposition, we only look at the discretization of the different operators on regular cells, that is cells that are not cut. The discretization on cut cells will be presented in Section 3.2.

3.1.1. Gradient, divergence, Laplacian and projections

Gradient, divergence and Laplacian operators are used throughout the equations. We use different types of spatial discretizations for computing the gradient and the divergence operators depending on where the initial variables are centered and how the result must be centered.

Gradient $\mathbf{G}$

The gradient operator $\mathbf{G}$ takes variables at cell centers and returns the gradient at cell faces.

$$(\mathbf{G}\varphi)_{x,i+\frac{1}{2}j} = \frac{\varphi_{i+1j} - \varphi_{ij}}{\Delta x} \tag{122}$$

On boundaries where we have a Dirichlet boundary condition $\varphi = b$, we do a linear interpolation to get

$$(\mathbf{G}\varphi)_{x,i+\frac{1}{2}j} = 2\frac{b_{i+\frac{1}{2}j} - \varphi_{ij}}{\Delta x} \tag{123}$$

When the tangential gradient needs to be computed, we use

$$(\mathbf{G}\varphi)_{z,i+\frac{1}{2}j} = \frac{1}{4}\left((\mathbf{G}\varphi)_{z,ij+\frac{1}{2}} + (\mathbf{G}\varphi)_{z,ij-\frac{1}{2}} + (\mathbf{G}\varphi)_{z,i+1j-\frac{1}{2}} + (\mathbf{G}\varphi)_{z,i+1j-\frac{1}{2}}\right) \tag{124}$$

On the boundary, we extrapolate the tangential gradients to second order as shown in Fig. 5.

Cell-centered gradient $\mathbf{G}_0$

The cell-centered operator $\mathbf{G}_0$ takes variables at cell centers and returns the gradient at cell centers.

$$\mathbf{G}_0 = Av^{F\to C}\mathbf{G} \tag{125}$$

where $Av^{F\to C}$ represents the following arithmetic average:

$$\left(Av^{F\to C}(\mathbf{G}\varphi)\right)_{x,ij} = \frac{(\mathbf{G}\varphi)_{x,i-\frac{1}{2}j} + (\mathbf{G}\varphi)_{x,i+\frac{1}{2}j}}{2} \tag{126}$$

Face-centered to cell-centered gradient $\mathbf{G}_{F\to C}$

The gradient $\mathbf{G}_{F\to C}$ takes variables at cell faces and returns the gradient at cell centers.

$$(\mathbf{G}_{F\to C}\varphi)_{x,ij} = \frac{\varphi_{i+\frac{1}{2}j} - \varphi_{i-\frac{1}{2}j}}{\Delta x} \tag{127}$$

Divergence D

The divergence D takes a vector variable $\mathbf{w} = (u, v)$ at cell faces and returns the divergence at cell centers.

$$D\mathbf{w}_{ij} = \frac{u_{i+\frac{1}{2}j} - u_{i-\frac{1}{2}j}}{\Delta x} + \frac{v_{ij+\frac{1}{2}} - v_{ij-\frac{1}{2}}}{\Delta z} \tag{128}$$

Cell-centered divergence D_0

The cell-centered divergence takes a vector variable at cell centers and returns the gradient at cell centers.

$$D_0 = DAv^{C\to F} \tag{129}$$

where $Av^{C\to F}$ represents the following arithmetic average:

$$\left(Av^{C\to F}u\right)_{i+\frac{1}{2}j} = \frac{u_{ij} + u_{i+1j}}{2} \tag{130}$$

Operator $\mathbb{L}_\rho$

The operator $\mathbb{L}_\rho$ is given by

$$\mathbb{L}_\rho = D\frac{1}{\rho}\mathbf{G} \tag{131}$$

Projections

The discretized projections are given by

$$\mathbb{Q}_\rho = \frac{1}{\rho}\mathbf{G}\mathbb{L}^{-1}_{\frac{\rho}{\eta_0}} D\eta_0 \tag{132}$$

$$\mathbb{P}_\rho = \mathbb{I} - \mathbb{Q}_\rho \tag{133}$$

$$\mathbb{Q}^0_\rho = \frac{1}{\rho}\mathbf{G}_0\mathbb{L}^{-1}_{\frac{\rho}{\eta_0}} D_0\eta_0 \tag{134}$$

$$\mathbb{P}^0_\rho = \mathbb{I} - \mathbb{Q}^0_\rho \tag{135}$$

To compute $\mathbb{Q}_\rho(\mathbf{w})$, for example, we introduce $\tilde{\mathbf{w}} = D(\eta_0\mathbf{w})$, and solve for φ

$$\mathbb{L}^H_{\frac{\rho}{\eta_0}}\varphi = \tilde{\mathbf{w}} \tag{136}$$

where $\mathbb{L}^H_{\frac{1}{\eta_0}} = D\eta_0 G$ is a Poisson operator with homogeneous boundary conditions and D^{PROJ} is the divergence D where the boundary conditions are assumed to be homogeneous on Neumann boundaries. Then, we find $\mathbb{Q}_\rho(\mathbf{w})$ by

$$\mathbb{Q}_\rho\mathbf{w} = \frac{1}{\rho}\mathbf{G}\varphi \tag{137}$$

3.1.2. Advective terms in the anelastic equations (31) and (32)

The operators presented above will now be used to compute the two advective terms in Eqs. (31) and (32). $\mathbf{A_d u}$ can be written in the following form:

$$\mathbf{A_d u} = \mathrm{div}(\mathbf{u}\otimes\mathbf{u}_d) + \mathrm{div}(\mathbf{u}_d\otimes(\mathbf{u}_p+\mathbf{u}_h)) - \mathbf{u}_d\cdot\mathrm{div}(\mathbf{u}) - (\mathbf{u}_p+\mathbf{u}_h)\cdot\mathrm{div}(\mathbf{u}_d) \tag{138}$$

$\mathbf{A_d u}$ and $\mathrm{div}(\tilde{\rho}\mathbf{u})$ and are made exclusively of divergence operators and need to be evaluated at half time steps. To retain the conservation of mass property, we choose the divergence D for discretizing these two terms and, therefore, we need to get $\mathbf{u}_d$, $\mathbf{u}$ and $\tilde{\rho}$ at face centers and at half time step.

Godunov advection procedure

In the Godunov advection procedure, we obtain the values at face centers and half time step by first extrapolating separately from the centers of the two adjacent cells using a Taylor series expansion

$$\tilde{\rho}^{n+\frac{1}{2}}_{ij,\pm,s} = \tilde{\rho}^n_{ij} \pm \frac{\Delta x_s}{2}\left(\frac{\partial\tilde{\rho}}{\partial x_s}\right)^n_{ij} + \frac{\Delta t}{2}\left(\frac{\partial\tilde{\rho}}{\partial t}\right)^n_{ij} \tag{139}$$

$$\mathbf{u}^{n+\frac{1}{2}}_{d,ij,\pm,s} = \mathbf{u}^n_{d,ij} \pm \frac{\Delta x_s}{2}\left(\frac{\partial\mathbf{u}_d}{\partial x_s}\right)^n_{ij} + \frac{\Delta t}{2}\left(\frac{\partial\mathbf{u}_d}{\partial t}\right)^n_{ij} \tag{140}$$

where the notation is illustrated in Fig. 3.

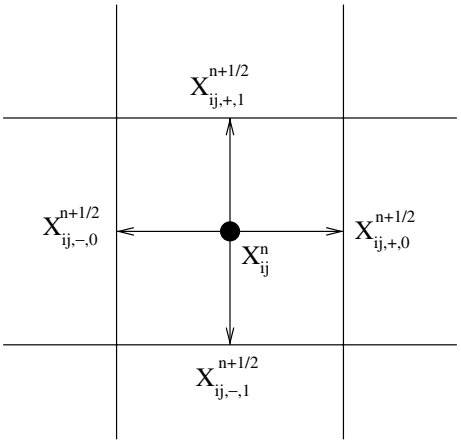

Fig. 3. Notation.

By replacing the time derivatives using either Eq. (31) or (32)

$$\left(\tilde{\rho}^{n+\frac{1}{2}}_{ij,\pm,s}\right) = \tilde{\rho}^{n}_{ij} \pm \frac{1}{2}\min\left\{\left(1 \mp \frac{\Delta t}{\Delta x_s}u^{n}_{ij}\right), 1\right\}(\Delta_{x_s}\tilde{\rho})^{n}_{ij} - \frac{\Delta t}{2\Delta x_{s'}}w^{n}_{ij}[\tilde{\rho}]^{n}_{x_{s'},ij} - \frac{\Delta t}{2}\tilde{\rho}^{n}_{ij}(D_0(\mathbf{u}^n))_{ij} - \frac{\Delta t}{2\eta_{0,ij}}\rho_{0,ij}(D(\eta_0\mathbf{u}^n_p))_{ij} + \frac{\Delta t}{2}\frac{N^2\rho_{0,ij}}{g}w^{n}_{ij} \tag{141}$$

$$\begin{aligned}(u^{n+\frac{1}{2}}_{d,ij,\pm,s}) = {} & u^{n}_{d,ij} \pm \frac{1}{2}\min\left\{\left(1 \mp u_{ij}\frac{\Delta t}{\Delta x_s}\right), 1\right\}(\Delta_{x_s}u_d)^{n}_{ij} - \frac{\Delta t}{2\Delta x_{s'}}w_{ij}[u_d]^{n}_{x_{s'}ij} \\ & - \frac{\Delta t}{2}(\mathbf{u}^{n}_{d,ij})_{x_s}\left(\mathbf{G}_{F\to C}\mathbf{u}^{n}_{pot}\right)_{x_s,ij} - \frac{\Delta t}{2\rho^{n}_{ij}}\left(\frac{\partial\pi^{n}_{H}}{\partial x_s}\right)_{ij}\delta_{s0} - \frac{\Delta t}{2\rho^{n}_{ij}}\left(\frac{\partial\pi^{n}_{I}}{\partial x_s}\right)_{ij} \\ & - \frac{\Delta t}{2\rho^{n}_{ij}}\left(\frac{\partial\psi^{n}}{\partial x_s}\right)_{ij} - \frac{\Delta t}{2}\mathbb{P}^0_0\left(\frac{1}{\rho^n}\mathbf{G}_0(\delta^n) + \mathbf{G}_0\left(\frac{\left|\mathbf{u}^{n}_{p} + \mathbf{u}_h\right|^2}{2}\right)\right)^{n}_{x_s,ij}\end{aligned} \tag{142}$$

where $s \neq s'$, δ_{s0} is a Dirac function

$$\delta_{s0} = \begin{cases} 1 & s = 1 \\ 0 & s \neq 1 \end{cases} \tag{143}$$

and w^{n}_{ij} is given by

$$w^{n}_{ij} = \left(w^{n}_{d,ij} + \left(Av^{F\to C}(w^{n}_{p})\right)_{ij}\right) \tag{144}$$

and the slopes are computed

- in the normal direction using

$$(\Delta_x u)^{n}_{ij} = \frac{u^{n}_{i+1j} - u^{n}_{i-1j}}{2}; \quad (\Delta_x\tilde{\rho})^{n}_{ij} = \frac{\tilde{\rho}^{n}_{i+1j} - \tilde{\rho}^{n}_{i-1j}}{2} \tag{145}$$

- in the tangential direction using

$$[u]^{n}_{ij} = u^{n}_{ij} - u^{n}_{ij-1}; \quad [\tilde{\rho}]^{n}_{ij} = \tilde{\rho}^{n}_{ij} - \tilde{\rho}^{n}_{ij-1} \qquad \text{if } w_{ij} > 0 \tag{146}$$

$$[u]^{n}_{ij} = u^{n}_{ij+1} - u^{n}_{ij}; \quad [\tilde{\rho}]^{n}_{ij} = \tilde{\rho}^{n}_{ij+1} - \tilde{\rho}^{n}_{ij} \qquad \text{if } w_{ij} < 0 \tag{147}$$

Then, the solution is upwinded to get the final value of the variables on face edges

$$u^{n+\frac{1}{2}}_{d,i+\frac{1}{2}j};\tilde{\rho}^{n+\frac{1}{2}}_{i+\frac{1}{2}j} = \begin{cases} u^{n+\frac{1}{2}}_{d,ij,+,0};\tilde{\rho}^{n+\frac{1}{2}}_{ij,+,0} & \text{if } u^{\text{edge}}_{i+\frac{1}{2}j} > 0 \\ u^{n+\frac{1}{2}}_{d,i+1j,-,0};\tilde{\rho}^{n+\frac{1}{2}}_{i+1j,-,0} & \text{if } u^{\text{edge}}_{i+\frac{1}{2}j} < 0 \\ \frac{1}{2}\left(u^{n+\frac{1}{2}}_{d,ij,+,0} + u^{n+\frac{1}{2}}_{d,i+1j,-,0}\right);\frac{1}{2}\left(\tilde{\rho}^{n+\frac{1}{2}}_{ij,+,0} + \tilde{\rho}^{n+\frac{1}{2}}_{i+1j,-,0}\right) & \text{if } u^{\text{edge}}_{i+\frac{1}{2}j} = 0 \end{cases} \tag{148}$$

Because the new anelastic velocity does not satisfy Eq. (9), we introduce a potential φ that verifies

$$\mathbb{L}_{\frac{1}{\eta_0}}\varphi = D\left(\eta_0 \mathbf{u}_d^{n+\frac{1}{2}}\right) \tag{149}$$

and we correct $\mathbf{u}_d^{n+\frac{1}{2}}$,

$$\mathbf{u}_d^{n+\frac{1}{2}} = \mathbf{u}_d^{n+\frac{1}{2}} - \mathbf{G}\varphi \tag{150}$$

The total velocity at face centers at half time steps is computed using

$$\mathbf{u}^{n+\frac{1}{2}} = \mathbf{u}_h + \mathbf{u}_d^{n+\frac{1}{2}} + \mathbf{u}_p^n \tag{151}$$

where the transverse components of $\mathbf{u}_h$ and $\mathbf{u}_p$ are computed by averaging the normal components in the same manner as the transverse gradient $\mathbf{G}$ is computed.

Computing $\mathbf{A_d u}$ *and* $\operatorname{div}(\tilde{\rho}\mathbf{u})$

Now, we have all the terms that are needed to compute the advective terms

$$[\operatorname{div}(\tilde{\rho}\mathbf{u})]^{n+\frac{1}{2}}_{ij} \approx \left[D\left(\tilde{\rho}^{n+\frac{1}{2}}\mathbf{u}^{n+\frac{1}{2}}\right)\right]_{ij} \tag{152}$$

$$[\mathbf{A_d u}]^{n+\frac{1}{2}}_{ij} \approx \left[D\left(\mathbf{u}^{n+\frac{1}{2}} \otimes \mathbf{u}_d^{n+\frac{1}{2}}\right)\right]_{ij} + \left[D\left(\mathbf{u}_d^{n+\frac{1}{2}} \otimes \left(\mathbf{u}_p^n + \mathbf{u}_h\right)\right)\right]_{ij} - \mathbf{u}^{n+\frac{1}{2}}_{d,ij}\left(D\mathbf{u}^{n+\frac{1}{2}}\right)_{ij} - \left(\mathbf{u}_p^n + \mathbf{u}_h\right)_{ij}\left(D\mathbf{u}_d^{n+\frac{1}{2}}\right)_{ij} \tag{153}$$

3.2. Discretization of the operators on cut cells

An embedded boundary (EB) formulation is used to model the orography, i.e. the mountain ranges. The mountain cuts cells as shown in Fig. 4 and some faces are cut while some others are completely covered. The fact that some faces are not full faces has consequences on how we evaluate the operators presented in Section 3.1 and this section presents what is done differently on the embedded boundary. This approach follows Johansen and Colella [17] for elliptic problems. For hyperbolic and parabolic problems, similar ideas have been used [1,25].

Gradient $\mathbf{G}$

The gradient in the normal direction is unchanged. However, for the tangential gradient, we need the value of the normal gradient on four faces, some of which might not be available on irregular cells. The missing gradients are, then, extrapolated to second order as shown in Fig. 5 and formula (124) remains unchanged.

Cell-centered gradient $\mathbf{G}_0$

In the average procedure, we need quantities at faces and, on some of the irregular cells, these quantities might not be available as a face might be covered. When one quantity is missing, we extrapolate to second order from the non-covered faces in the normal direction and then proceed to the arithmetic averaging as in (126).

Divergence D

When we had only regular cells, D ensured that we had a conservative discretization of the divergence operator. However, if we used Eq. (128) when the cell is not regular, we would lose the conservative property.

To find the expression of the conservative divergence on cut cells, we average over the volume of the cell and then use Stokes' theorem to transform a volume integral into a surface integral so that we recover a flux balance

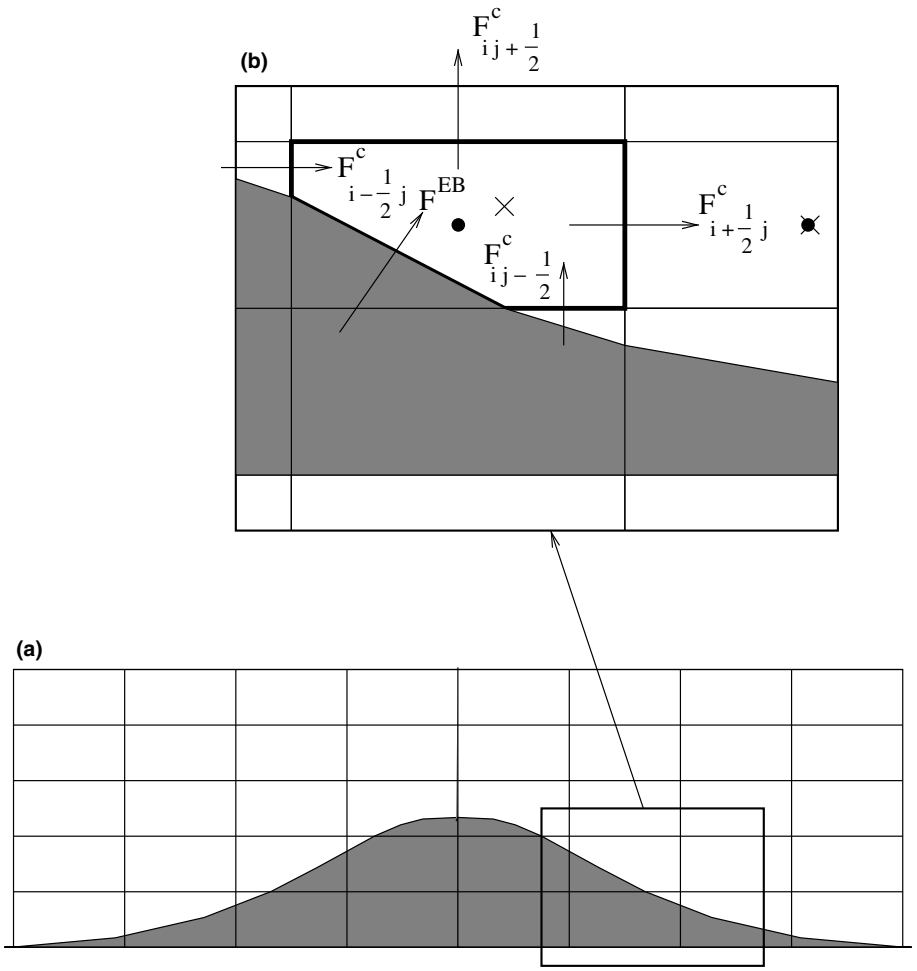

Fig. 4. Schematics of the embedded boundary with cut cells.

$$\nabla \cdot \mathbf{F}(\mathbf{u}) \approx \frac{1}{V}\int_V \nabla \cdot \mathbf{F}\,\mathrm{d}V \tag{154}$$

$$\approx \frac{1}{V}\oint_S \mathbf{F}\cdot\mathbf{n}\,\mathrm{d}S \tag{155}$$

$$\approx \frac{1}{\kappa_{ij}}\left[\frac{\alpha_{i+\frac{1}{2}j}F^c_{i+\frac{1}{2}j}-\alpha_{i-\frac{1}{2}j}F^c_{i-\frac{1}{2}j}}{\Delta x}+\frac{\alpha_{ij+\frac{1}{2}}F^c_{ij+\frac{1}{2}}-\alpha_{ij-\frac{1}{2}}F^c_{ij-\frac{1}{2}}}{\Delta z}+\alpha^{EB}F^{EB}\right] \tag{156}$$

where the superscript c represents quantities taken at the centroid of the faces, which may be different from the center of the face, and the superscript EB represents the quantities at the embedded boundary. $\alpha_{i+\frac{1}{2}j}$ is the area fraction of the face $(i+\frac{1}{2}j)$, defined as the ratio of the actual face area over the face area of the regular mesh spacing in this direction, and κ_{ij} is the volume fraction defined as the ratio of the volume of the cell over the volume of a regular rectangular cell. $\mathbf{F}_{i+\frac{1}{2}j}$ is the flux on face $(i+\frac{1}{2}j)$ and is illustrated in Fig. 4(b).

Eq. (156) gives an easy expression to compute the divergence of a flux on a cut-cell. Note that when the cell is regular, i.e. $\alpha = 1$, $\kappa = 1$ and $\alpha^{EB} = 0$, we recover the classical expression for the divergence of a vector. This expression is however not sufficient as the volume fraction κ has the potential of becoming arbitrarily small, posing major accuracy and stability problems. When using the divergence operator to solve a Poisson's equation for example, multiplying both sides of the equation by κ removes the potential singularity. This approach is not possible for an explicit method.

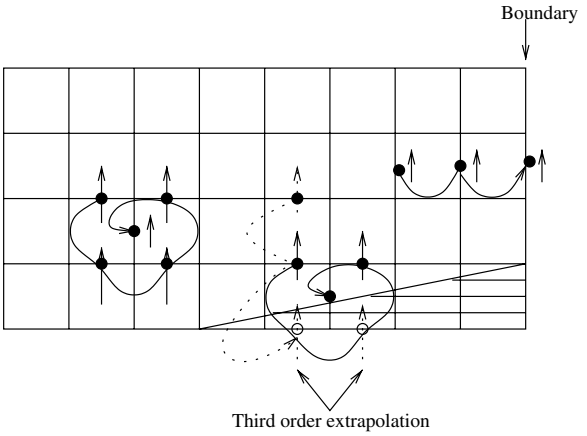

Fig. 5. Tangential gradient.

Redistribution

When computing the advective terms in a complex PDE, we eliminate κ in the denominator of (156) by using a mixed update of the form

$$\nabla \cdot \mathbf{F}(\mathbf{u}) = \kappa \nabla^{\mathrm{C}} \cdot \mathbf{F}(\mathbf{u}) + (1-\kappa)\nabla^{\mathrm{NC}} \cdot \mathbf{F}(\mathbf{u}) \tag{157}$$

where $\nabla^{\mathrm{C}} \cdot \mathbf{F}$ is the conservative divergence as expressed in Eq. (156) and $\nabla^{\mathrm{NC}} \cdot \mathbf{F}$ is the non-conservative divergence that has the same expression as the divergence on regular rectangular cells, where the data is taken at face centers and extrapolated to covered faces if needed. This update (157) is not conservative, so we compute the mass δM that was added by using the non-conservative update

$$\delta M = \kappa\left[\nabla \cdot \mathbf{F}(\mathbf{u}) - \nabla^{\mathrm{C}} \cdot \mathbf{F}(\mathbf{u})\right] \tag{158}$$

$$= \kappa(1-\kappa)\left[\nabla^{\mathrm{NC}} \cdot \mathbf{F}(\mathbf{u}) - \nabla^{\mathrm{C}} \cdot \mathbf{F}(\mathbf{u})\right] \tag{159}$$

and redistribute it to adjacent cells to ensure overall conservation of mass [3,6,29].

The complications arising from the presence of cut-cells are widely compensated by the advantages of having an underlying rectangular grid on the computational domain: the grid generation is stable and well-understood, and the coupling to structured AMR is straightforward.

Extrapolating to covered faces

To compute the non-conservative divergence in Eq. (157) that takes data on face centers, we need values on covered faces if there are any covered faces in the cut-cell. These values are extrapolated from adjacent faces and cells as pictured in Fig. 6. For example, to extrapolate the quantity W on the covered face shown in Fig. 6, we compute

$$\left(W^{n+\frac{1}{2}}_{i-\frac{1}{2},j}\right)^{+}_{\mathbf{A}} = W^{n}_{i+1,j} + \frac{1}{2}\left(-3 - \frac{\Delta t}{\Delta x}u^{n}_{i+1,j}\right)(\Delta_x W)^{n}_{i+1,j} - \frac{\Delta t}{2\Delta z}w^{n}_{i+1j}[W]^{n}_{z,i+1j} - \frac{\Delta t}{2}R^{n}_{i+1j} \tag{160}$$

$$\left(W^{n+\frac{1}{2}}_{i-\frac{1}{2},j}\right)^{+}_{\mathbf{B}} = W^{n}_{i-1,j+1} + \frac{1}{2}\min\left\{\left(1 - \frac{\Delta t}{\Delta x}u^{n}_{i-1,j+1}\right), 1\right\}(\Delta_x W)^{n}_{i-1,j+1} - (W^{n}_{i-1,j+2} - W^{n}_{i-1,j+1}) - \frac{\Delta t}{2\Delta z}w^{n}_{i-1j+1}[W]^{n}_{z,i-1j+1} - \frac{\Delta t}{2}R^{n}_{i-1j+1} \tag{161}$$

where W satisfies an equation of the form

$$\frac{\partial W}{\partial t} + \mathbf{u} \cdot \mathbf{grad}(W) + R(x,z,t) = 0 \tag{162}$$

The final density on the covered face is taken to be

$$\left(W^{n+\frac{1}{2}}_{i-\frac{1}{2},j}\right)^{\pm} = n_x^2\left(W^{n+\frac{1}{2}}_{i-\frac{1}{2},j}\right)^{\pm}_{\mathbf{A}} + n_z^2\left(W^{n+\frac{1}{2}}_{i-\frac{1}{2},j}\right)^{\pm}_{\mathbf{B}} \tag{163}$$

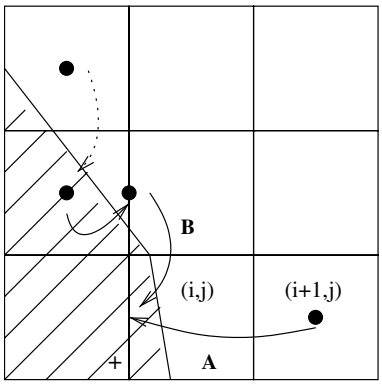

Fig. 6. Schematics of the extrapolation scheme to a covered face.

where n_x and n_z are the components of the normal in the horizontal and vertical direction. Another extrapolation technique is presented in [8].

4. Results

4.1. Perturbational gravity-wave test problem

In the asymptotic analysis of Section 1, we showed that we could extract a finite collection of discrete traveling gravity waves from the fully compressible equations in the limit of low Mach and Froude numbers and small aspect ratio. The details of the derivation can be found in the Appendix.

We set up this example to verify the asymptotics results numerically, using the full compressible equations. The problem is initialized to be a traveling wave in the fastest mode and, following the asymptotic analysis, we expect to see the wave propagate and stay in the fastest mode.

4.1.1. Initialization

The pressure π_H and the solenoidal velocity are initialized as

$$\hat{u}_d(x,z,t=0) = G(x)r^0(z) \tag{164}$$

$$\hat{\pi_H}(x,z,t=0) = c^0\hat{u}_d(x,z,t=0) \tag{165}$$

or identically for the pressure π_H,

$$\pi_H(x,z,t=0) = \rho_0 c^0 u_d(x,z,t=0) \tag{166}$$

where r^0 is the eigenvector associated with the fastest mode and c^0 is the speed of the fastest wave. $G(x)$ is a Gaussian function

$$G(x) = \frac{\alpha}{\sqrt{2\pi}\sigma}\exp\left(-\frac{(x-x_0)^2}{2\sigma^2}\right) \tag{167}$$

The remainder of the initialization must be done carefully to avoid artificially sending energy in modes that are not the fastest mode. First, the vertical component of the solenoidal velocity is initialized using the anelastic constraint (9)

$$w_d(x,z,t=0) = \frac{1}{\eta_0}\int_0^z \eta_0\left(\frac{c^{0^2}}{c_0^2}-1\right)\frac{\partial u_d}{\partial x}\mathrm{d}z \tag{168}$$

When computing the discrete integral, particular care needs to be taken to ensure that the discrete $\mathbf{u}_d$ satisfies the condition

$$D\eta_0\mathbf{u}_d = 0 \tag{169}$$

The potential velocity is then initialized using Eq. (66). We use the fact that $\mathbf{u}_p$ is a gradient

$$\mathbf{u}_p = \mathbf{grad}\,\varphi \tag{170}$$

and this yields

$$\mathbb{L}_{\frac{\perp}{\eta_0}}\varphi = -\frac{\eta_0}{\rho_0 c_0^2}\frac{\partial \pi_H}{\partial t} \tag{171}$$

The time derivative of the pressure π_H is found by using the relationship derived in Appendix

$$\lambda^0 \frac{\partial \hat{\pi}_H}{\partial t} + \frac{\partial \hat{u}_d}{\partial x} = 0 \tag{172}$$

since all the quantities are taken along the first eigenmode. φ then verifies

$$\mathbb{L}_{\frac{\perp}{\eta_0}}\varphi = -\eta_0 \frac{c^{0\,2}}{c_0^2}\frac{\partial u_d}{\partial x} \tag{173}$$

The rest of the quantities are initialized according to their definitions.

4.1.2. Results

In this example, we use different domain sizes and different grid refinements to verify the asymptotics, as shown in Table 2.

Figs. 7(a)–(c) show that we obtain a traveling wave solution for aspect ratios of 0.025 and under. Figs. 8 and 9(a) show that the decay in the amplitude of the solution and the amount of energy that gets transfered into the slow modes decrease as the aspect ratio decreases, as this means that the asymptotic assumptions are better verified. Fig. 9(b) shows that the convergence is first order.

Fig. 7(d) shows that we are not quite in the asymptotics regime for $\varepsilon = 0.05$. The traveling wave gets deformed at the beginning of the simulation on the left of the propagating front and then this deformed wave propagates. The decay in amplitude as the wave propagates is much larger than in the cases where we are in the asymptotic regime, and a much larger part of the motion gets transferred from the fastest mode to the slow modes.

However, it is to be noted that even when the asymptotic assumptions hold loosely (as is the case with $\varepsilon = 0.05$), the percentage of the solution that gets transferred into the slow modes is under 4% for π_H and under 6% for u_d on a 128×64 grid. We also notice that the smaller ε is, the closer the propagation velocity is to c^0 with a very good match for $\varepsilon = 0.0125$ as seen in Fig. 8.

4.2. Mountain Lee waves

Our algorithm is now tested on the classical examples of gravity waves found in [10,12]. In these examples, a uniform wind with a speed of 20 m/s passes over a 600 m, as pictured in Fig. 10. The mountain has the shape of a "witch of Agnesi"

$$z_{\text{Mountain}}(x) = \frac{ha}{(x - x_0)^2 + a^2} \tag{174}$$

where $a = 10$ km is the mountain width, $h = 600$ m is the mountain height and $x_0 = 72$ km is the position of the mountain crest.

The numerical domain measures 180 km × 12.8 km and there is a 6.3 km deep sponge layer on top of the domain and a 30 km deep sponge layer on either side of the domain. The sponge layers damp the reflection of spurious gravity waves on the top and the sides of the domain.

Table 2
Different cases used for the asymptotic analysis

	$\varepsilon = 0.05$	$\varepsilon = 0.025$	$\varepsilon = 0.0125$	$\varepsilon = 0.00625$
Domain length (km)	256	512	1024	2048
Domain height (km)	12.8	12.8	12.8	12.8

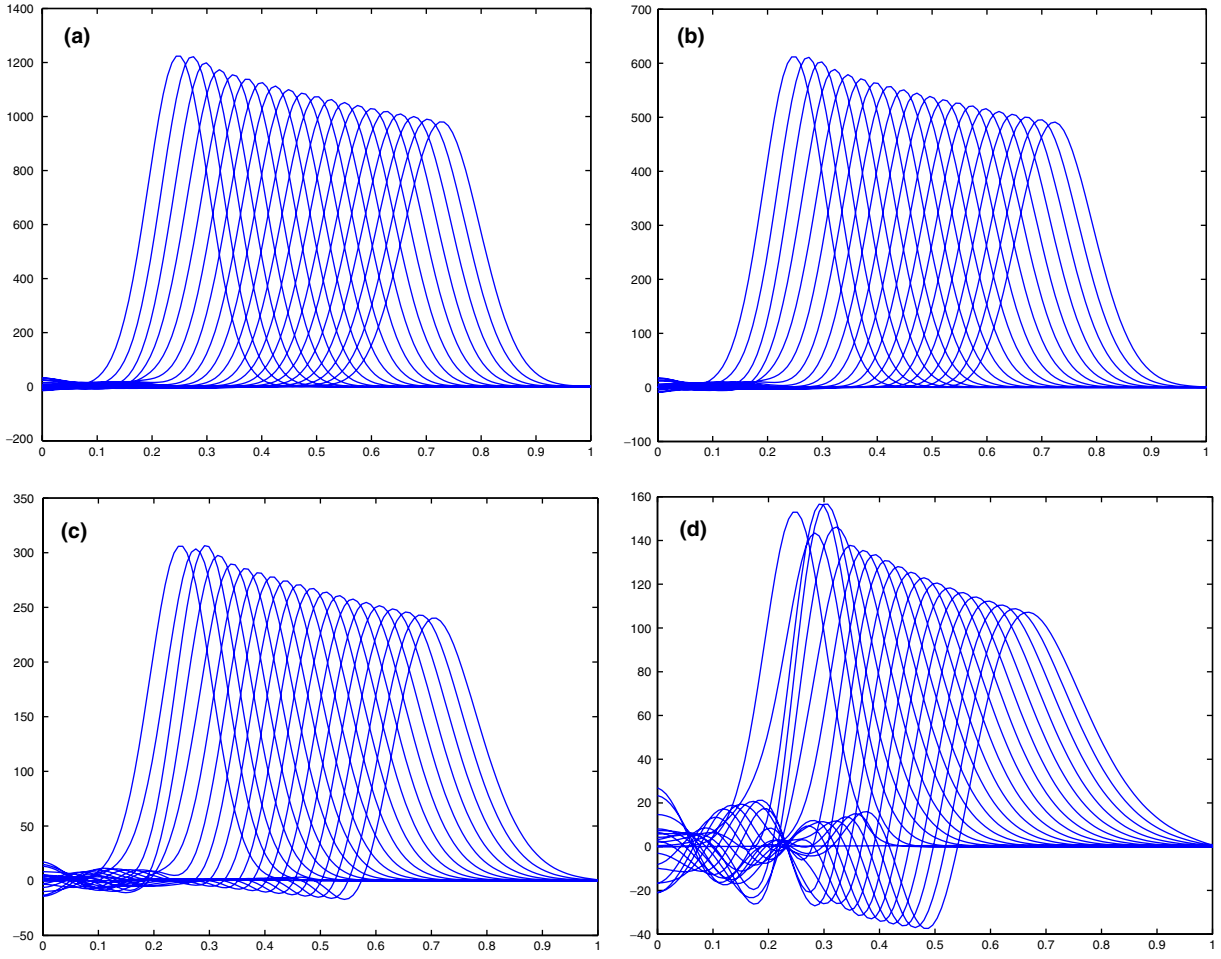

Fig. 7. π_H history on a 128×64 grid for different aspect ratios: (a) $\varepsilon = 0.00625$, (b) $\varepsilon = 0.0125$, (c) $\varepsilon = 0.025$, and (d) $\varepsilon = 0.05$.

The atmosphere is a two-layered atmosphere and, in each layer, the Brunt–Väisälä frequency is a constant that takes one of these two values 0.01 s^{-1} or 0.02 s^{-1}. The initial background density is given by

$$\rho_0(z) = \rho_{0i} \exp\left(-\frac{N_i^2(z - z_i)}{g}\right)\left(\frac{1 - (\gamma - 1)C_i \exp\left(-\frac{N_i^2 z}{g}\right)}{1 - (\gamma - 1)C_i \exp\left(-\frac{N_i^2 z_i}{g}\right)}\right)^{\left(\frac{1}{\gamma - 1}\right)} \tag{175}$$

where $i \in \{L, U\}$, $z_L = 0$, $z_U = H$ and the constants C_i are given by

$$C_L = -\frac{\frac{2\rho_0 g^2}{\gamma p_0 N_L^2}}{1 - (\gamma - 1)\frac{2\rho_0 g^2}{\gamma p_0 N_L^2}} \tag{176}$$

$$C_U = C_0 \exp\left(-\frac{N_L^2 H}{g}\right)\left(\frac{N_L}{N_U}\right)^2 \frac{1}{1 - (\gamma - 1)C_L \exp\left(-\frac{N_L^2 H}{g}\right)} \tag{177}$$

The initial background pressure is then given by the hydrostatic relation (7).

According to linear theory, there are four possible tuned and detuned cases that can occur in a two-layered atmosphere, yielding gravity waves in some cases, depending on the position (top or bottom) of the layer with higher stability and on the value of the phase shift between the ground and the interface between the two lay-

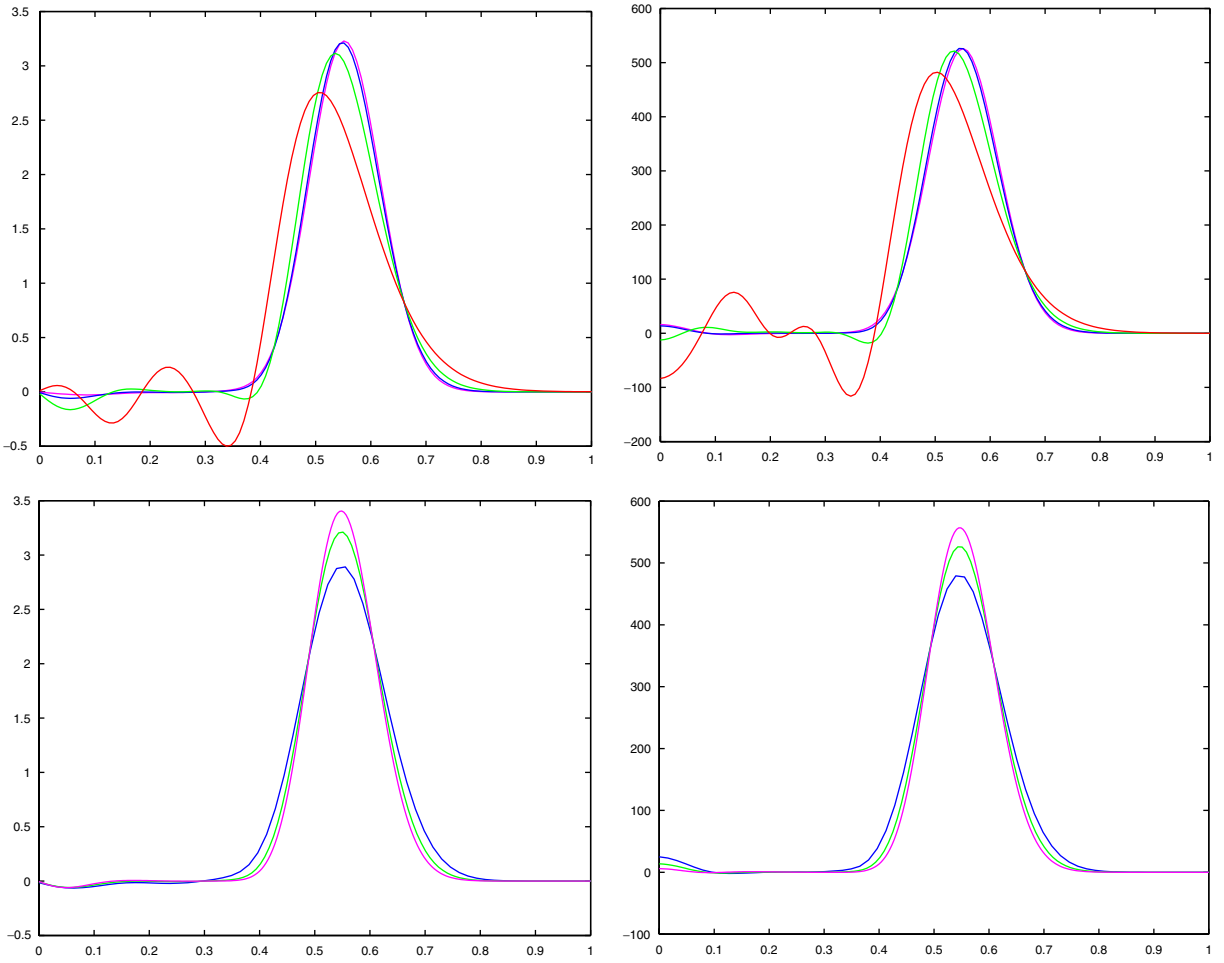

Fig. 8. u_d (left) and π_H (right), above for different aspect ratios holding the grid size fixed at 128×64: 0.05 (red), 0.025 (green), 0.0125 (blue), 0.00625 (pink); and below for different resolutions holding the aspect ratio fixed at 0.0125: 64×32 (blue), 128×64 (green), 256×128 (pink). (For interpretation of the references in color in this figure legend, the reader is referred to the web version of this article.)

ers. Table 3 presents a summary of the four possible cases. In Table 3, N_L is the Brunt–Väisälä frequency of the lower layer, N_U is the Brunt–Väisälä frequency of the upper layer and H is the height of the interface.

Fig. 11 represents cases (a)–(c) shown in Table 3. Here, the grid spacing is 128×64 cells and the time step is $\Delta t = 15$ s. The benchmark results from Durran were run using a small time step of 5 s and a large time step of 10 s. Table 4 shows that the time step that we have chosen satisfies the CFL condition for the fastest gravity wave whose speed is computed using the analysis shown in Appendix. Note that similar examples were run by Bonaventura [4] and Rosatti et al. [31] using a time step that seems to be determined by the advective CFL condition. They use a semi-Lagrangian cut-cell method that treats implicitly both the acoustic and the gravity waves. In a further study [14], we have used the approach described here to develop a filtering method that allows time steps larger than those imposed by the fast gravity waves, leading to methods for which the time step is comparable to the advective CFL condition.

Fig. 11 compares qualitatively well with Fig. 2 from Durran [10]. For case (c), the match is remarkable and the positions of the crest of the waves are almost identical. For cases (a) and (b), the match is also very good. The waves have the same wavelength than the one found in Durran, but their amplitudes differ slightly. For case (b), we also recover the main features of the isentropes: the amplitudes of the gravity waves increase with height while in the lower layer and decrease with height while in the upper layer, the sag starts at the crest of the mountain and ends near the foot of the mountain before the gravity waves start to form, and the sag is replaced by a big jump in the upper layer.

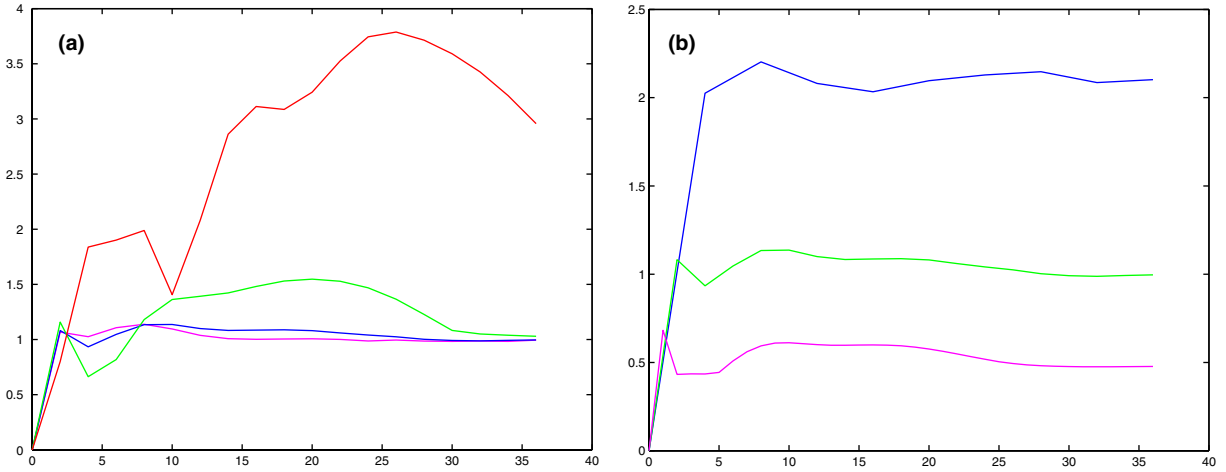

Fig. 9. Percentage of the π_H solution that gets transfered from the fast mode to the slows modes; (a) for different aspect ratios holding the grid size fixed at 128×64: 0.05 (red), 0.025 (green), 0.0125 (blue), 0.00625 (pink), (b) for different grid resolutions holding the aspect ratio fixed at 0.0125: 64×32 (blue), 128×64 (green), 256×128 (pink). (For interpretation of the references in color in this figure legend, the reader is referred to the web version of this article.)

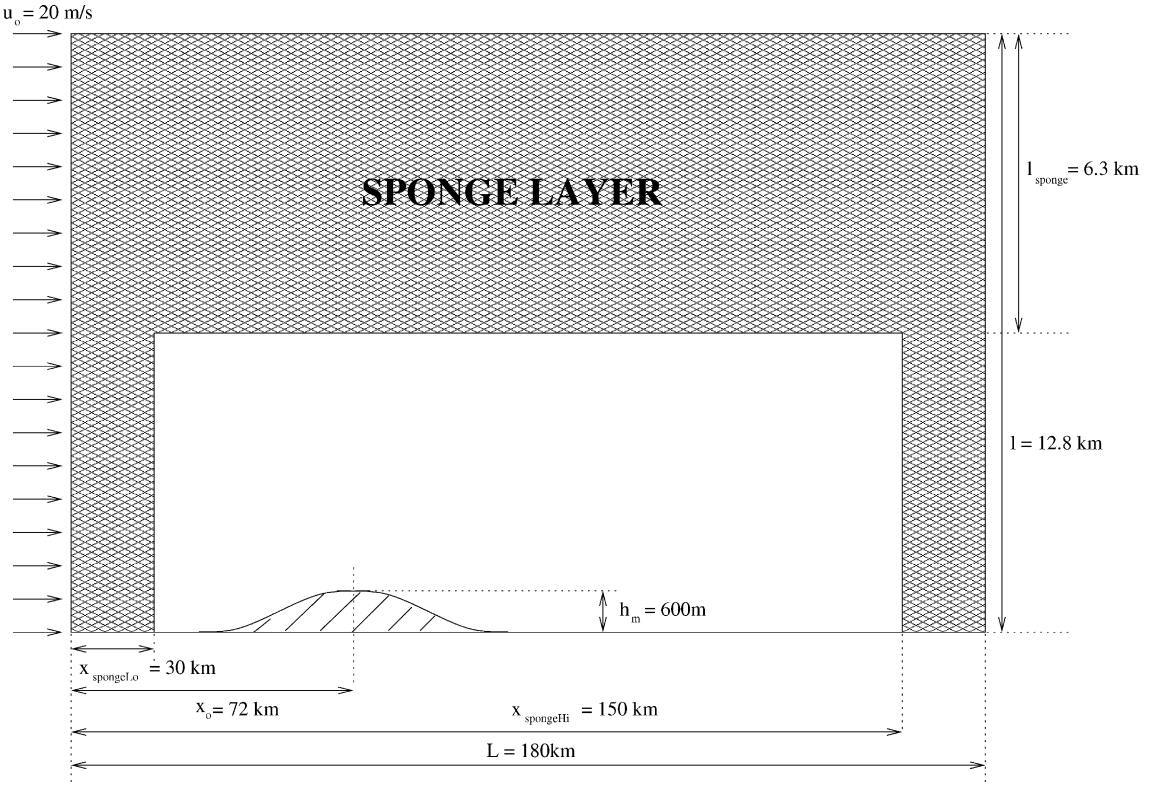

Fig. 10. Schematic of the parameters.

Table 3
Position of the interface and wave response for different tuned and detuned cases

Case	N_L (s^{-1})	N_U (s^{-1})	H (m)	Amplitude of waves
(a)	0.02	0.01	1571	Weak
(b)	0.02	0.01	3142	Strong
(c)	0.01	0.02	3142	Strong

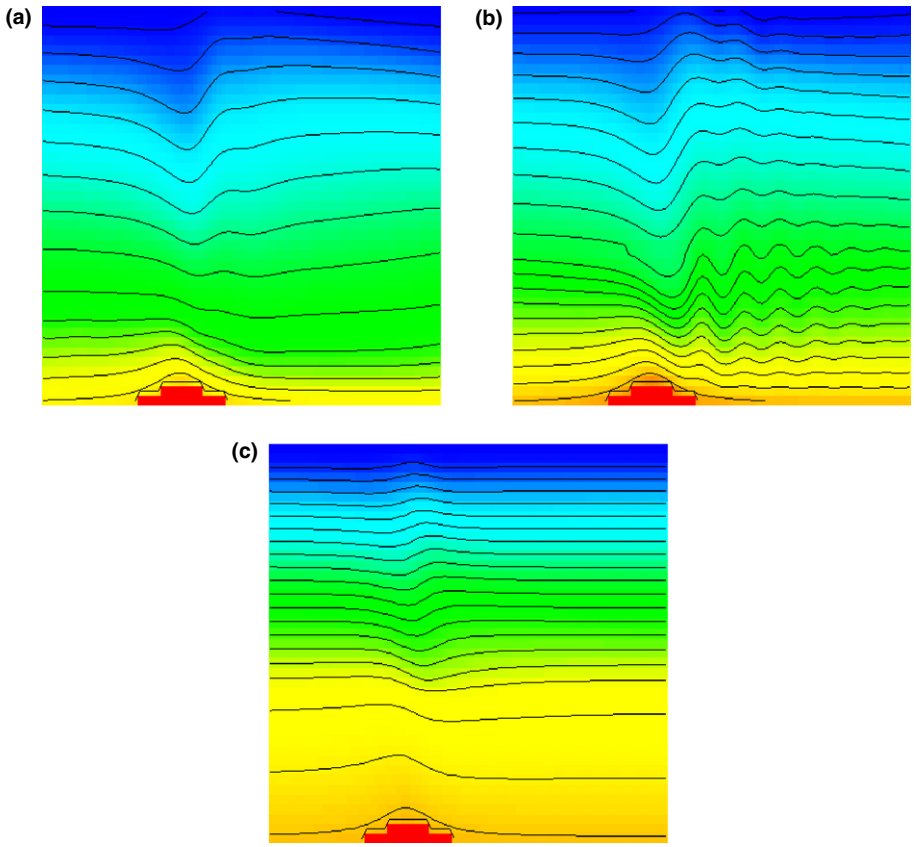

Fig. 11. Isentropes for a two-layered atmosphere flowing over a 600-m high mountain at $t = 10{,}000$ s. (a) Interface at 1571 m, one-quarter wavelength, (b) interface at 3141 m, one-half wavelength and (c) interface at 3141 m, one-quarter wavelength.

Table 4
Speed of fastest gravity wave c_{gw} and maximum time step for the lee-waves examples

	$N_L < N_U$		$N_U < N_L$
	Quarter wavelength	Half wavelength	Quarter wavelength
c_{gw} (m/s)	74	80	59
Δt (s)	19.08	17.62	23.49

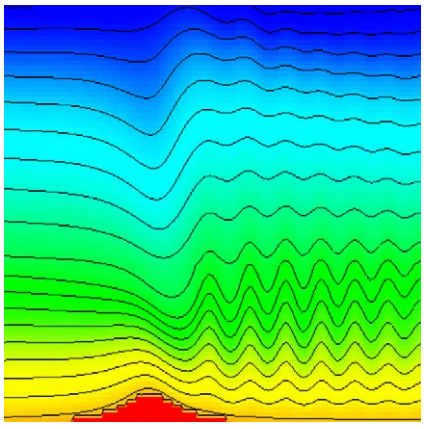

Fig. 12. Case (b) solved on a 256×128 grid.

Case (b) is also run on a 256×128 grid with a time step of $\Delta t = 7.5$ s as shown in Fig. 12. The wavelengths and the nominal position of the isentropes are identical for the finer and coarser resolution. However, for the finer resolution, the amplitudes of the gravity waves do not decay as fast away from the mountain as they do in Fig. 11(b).

5. Conclusion

We developed a numerical method for low-Mach/low-Froude number flows in a continuously stratified atmosphere. The numerical algorithm uses a splitting to separate the fast acoustic dynamics from the slower anelastic dynamics. In the limit of small Mach number and small aspect ratio, we recover an anelastic system of equations, with an inhomogeneous constraint given by (66). The acoustic waves are treated implicitly while the advective transport of the solenoidal velocity field is computed using explicit upwind methods, in an overall semi-implicit discretization of the splitting. The resulting formulation, combined with a vertical normal-mode analysis, provides a clear analytic separation of the acoustic, advective, and fast buoyant time scales in which the full problem, as well as the resulting sub-problems in the semi-implicit discretization, have well-posed formulations as boundary-value problems. Based on this approach, we developed a numerical method using a cut cell discretization of orography, and obtained results that compare very well with the classical gravity wave results presented in [10]. This splitting has been applied in [14] to obtain a method for which the time step can exceed by a substantial amount that obtained from the CFL condition imposed by the fastest gravity waves. Some of the further applications for this method include adaptive mesh refinement since the boundary-value problem for the component subproblems in the splitting are well-posed, and higher-order predictor–corrector step methods [26] because the different gravity modes are separated very cleanly.

Acknowledgement

We would like to acknowledge Dr. Joseph Tribbia for suggesting that we look at the vertical normal mode analysis.

Appendix. Determination of the time step and of the fastest gravity wave speed

The splitting allows to isolate and treat implicitly acoustic waves. Therefore, the speed of the fastest gravity wave c_{gw} is now setting a constraint on the time step

$$\Delta t < \frac{\Delta x}{c_{\mathrm{gw}}} \tag{178}$$

The fast gravity waves that are described by the asymptotic assumptions of Section 1 are horizontal traveling waves whose dynamics is mainly described by the solenoidal part of the flow, that is Eqs. (20) and (21) that can be rewritten

$$\frac{\partial \tilde{\rho}}{\partial t} + \rho_0 w \left[\frac{1}{\rho_0} \frac{\mathrm{d}\rho_0}{\mathrm{d}z} - \frac{1}{\eta_0} \frac{\mathrm{d}\eta_0}{\mathrm{d}z} \right] = -\mathrm{div}(\tilde{\rho}\mathbf{u}) - \frac{\rho_0}{\eta_0} \mathrm{div}(\eta_0 \mathbf{u}_p) \tag{179}$$

$$\frac{\partial u_d}{\partial t} + \frac{1}{\rho} \frac{\partial \pi_H}{\partial x} = -(\mathbf{A}_d \mathbf{u})_x - \frac{1}{\rho} \frac{\partial \pi_I}{\partial x} - \left[\mathbb{P}_0 \left(\frac{1}{\rho} \mathbf{grad}\, \delta + \mathbf{grad} \frac{|\mathbf{u}_p + \mathbf{u}_h|^2}{2} \right) \right]_x \tag{180}$$

Note, that for other regimes, the gravity waves do propagate in all directions.

We want the right-hand sides of Eqs. (179) and (180) to be small so that we can recover the classical system of equations for traveling waves. Analyzing the orders of magnitude of the different terms shows that $\frac{\rho_0}{\eta_0}\mathrm{div}(\eta_0 \mathbf{u}_p)$ is the dominant term in Eq. (179) and that, from Eq. (23), $\frac{\rho_0}{\eta_0}\mathrm{div}(\eta_0 \mathbf{u}_p) + \frac{1}{c_0^2}\frac{\partial \pi_H}{\partial t}$ is small. Therefore, we subtract $\frac{1}{c_0^2}\frac{\partial \pi_H}{\partial t}$ to both sides of Eq. (179)

$$\frac{\partial\tilde{\rho}}{\partial t}-\frac{1}{c_0^2}\frac{\partial\pi_H}{\partial t}+w\rho_0\left[\frac{1}{\rho_0}\frac{\mathrm{d}\rho_0}{\mathrm{d}z}-\frac{1}{\gamma p_0}\frac{\mathrm{d}p_0}{\mathrm{d}z}\right]=-\mathrm{div}(\tilde{\rho}\mathbf{u})-\left(\frac{\rho_0}{\eta_0}\mathrm{div}(\eta_0\mathbf{u}_p)+\frac{1}{c_0^2}\frac{\partial\pi_H}{\partial t}\right) \tag{181}$$

$$\frac{\partial u_d}{\partial t}+\frac{1}{\rho}\frac{\partial\pi_H}{\partial x}=-(\mathbf{A}_d\mathbf{u})_x-\frac{1}{\rho}\frac{\partial\pi_I}{\partial x}-\left[\mathbb{P}_0\left(\frac{1}{\rho}\mathbf{grad}\,\delta+\mathbf{grad}\frac{|\mathbf{u}_p+\mathbf{u}_h|^2}{2}\right)\right]_x \tag{182}$$

Using Eqs. (25) and (33) along with the definition of the Brunt Väisälä frequency $N=\sqrt{-g\left[\frac{1}{\rho_0}\frac{\mathrm{d}\rho_0}{\mathrm{d}z}-\frac{1}{\gamma p_0}\frac{\mathrm{d}p_0}{\mathrm{d}z}\right]}$, we obtain

$$\begin{aligned}-\frac{\eta_0 g}{\rho_0 N^2}\left(\frac{1}{g}\frac{\partial}{\partial z}+\frac{1}{c_0^2}\right)\frac{\partial\pi_H}{\partial t}-\eta_0 w&=R^*_{\pi_H}\\&=-\frac{\eta_0 g}{\rho_0 N^2}\mathrm{div}(\tilde{\rho}\mathbf{u})-\frac{\eta_0 g}{\rho_0 N^2}\left(\frac{\rho_0}{\eta_0}\mathrm{div}(\eta_0\mathbf{u}_p)+\frac{1}{c_0^2}\frac{\partial\pi_H}{\partial t}\right)\end{aligned} \tag{183}$$

$$\begin{aligned}\frac{\partial u}{\partial t}+\frac{1}{\rho_0}\frac{\partial\pi_H}{\partial x}&=R_u\\&=-(\mathbf{A}_d\mathbf{u})_x-\frac{1}{\rho}\frac{\partial\pi_I}{\partial x}-\left(\frac{1}{\rho}-\frac{1}{\rho_0}\right)\frac{\partial\pi_H}{\partial x}-\left[\frac{1}{\rho}\frac{\partial\delta}{\partial x}+\frac{\partial}{\partial x}\left(\frac{|\mathbf{u}_p+\mathbf{u}_h|^2}{2}\right)\right]\end{aligned} \tag{184}$$

Formal linear analysis shows that the two right hand-side terms $R^*_{\pi_H}$ and R_u are either quadratic in the perturbations or small because either the Mach number or the Froude number is small.

The idea is now to obtain a wave equation with variables x and t while averaging continuously the vertical variable z. First, differentiate Eq. (183) with respect to z,

$$\begin{aligned}\mathscr{L}_z\frac{\partial\pi_H}{\partial t}+\frac{\partial\eta_0 u_d}{\partial x}&=R_{\pi_H}\\&=-\frac{\partial}{\partial z}\left\{\frac{\eta_0 g}{\rho_0 N^2}\left[div(\tilde{\rho}u)+\frac{1}{c_0^2}\frac{\partial\pi_H}{\partial t}\right]+\frac{g}{N^2}\mathrm{div}(\eta_0\mathbf{u}_p)\right\}\\&\quad+\mathrm{div}(\eta_0\mathbf{u}_p)+\frac{\eta_0}{\rho_0 c_0^2}\frac{\partial\pi_H}{\partial t}-\frac{\partial\eta_0 u_p}{\partial x}\end{aligned} \tag{185}$$

$$\begin{aligned}\frac{\partial u_d}{\partial t}+\frac{1}{\rho_0}\frac{\partial\pi_H}{\partial x}&=R_u\\&=-\left((\mathbf{A}_d\mathbf{u})_x+\frac{1}{\rho}\frac{\partial\pi_I}{\partial x}+\left(\frac{1}{\rho}-\frac{1}{\rho_0}\right)\frac{\partial\pi_H}{\partial x}+\frac{\partial u_p}{\partial t}+\left[\frac{1}{\rho}\frac{\partial\delta}{\partial x}+\frac{\partial}{\partial x}\left(\frac{|\mathbf{u}_p+\mathbf{u}_h|^2}{2}\right)\right]\right)\end{aligned} \tag{186}$$

where we have added $\frac{\eta_0}{\rho_0 c_0^2}\frac{\partial\pi_H}{\partial t}$ to both sides of Eq. (185) and used

$$\frac{\partial\eta_0 w}{\partial z}+\frac{\partial\eta_0 u}{\partial x}=\mathrm{div}(\eta_0\mathbf{u}_p) \tag{187}$$

and where

$$\mathscr{L}_z=-\frac{\partial}{\partial z}\left[\frac{\eta_0 g}{\rho_0 N^2}\left(\frac{1}{g}\frac{\partial}{\partial z}+\frac{1}{c_0^2}\right)\right]+\frac{\eta_0}{\rho_0 c_0^2}=-\xi\left[\frac{\partial}{\partial z}\zeta\frac{\partial}{\partial z}+\chi\right] \tag{188}$$

with

$$\xi=\exp\left(-\int_0^z\frac{g}{c_0^2}\mathrm{d}z\right) \tag{189}$$

$$\zeta=\frac{\eta_0}{\rho_0 N^2}\exp\left(\int_0^z\frac{g}{c_0^2}\mathrm{d}z\right) \tag{190}$$

$$\chi=\frac{\eta_0}{\rho_0 c_0^2}\left[(\gamma-1)\frac{g^2}{N^2 c_0^2}-1\right]\exp\left(\int_0^z\frac{g}{c_0^2}\mathrm{d}z\right) \tag{191}$$

Introduce the following change of variables:

$$\hat{\pi}_H = \sqrt{\frac{\eta_0}{\rho_0 \xi}}\pi_H \tag{192}$$

$$\hat{u}_d = \sqrt{\frac{\rho_0 \eta_0}{\xi}}u_d \tag{193}$$

$$\hat{\mathscr{L}}_z = \sqrt{\frac{\rho_0}{\eta_0 \xi}}\mathscr{L}_z\sqrt{\frac{\rho_0 \xi}{\eta_0}} \tag{194}$$

$$\hat{R}_{\pi_H} = \sqrt{\frac{\rho_0}{\eta_0 \xi}}R_{\pi_H} \tag{195}$$

$$\hat{R}_u = \sqrt{\frac{\rho_0 \eta_0}{\xi}}R_u \tag{196}$$

and Eqs. (183) and (184) become

$$\begin{aligned}\hat{\mathscr{L}}_z \frac{\partial \hat{\pi}_H}{\partial t} + \frac{\partial \hat{u}_d}{\partial x} &= \hat{R}_{\pi_H} \\ &= -\sqrt{\frac{\rho_0}{\eta_0 \xi}}\frac{\partial}{\partial z}\left\{\frac{\eta_0 g}{\rho_0 N^2}\left[\operatorname{div}(\tilde{\rho}\mathbf{u}) + \frac{1}{c_0^2}\frac{\partial \pi_H}{\partial t}\right] + \frac{g}{N^2}\operatorname{div}(\eta_0 \mathbf{u}_p)\right\} \\ &\quad + \sqrt{\frac{\rho_0}{\eta_0 \xi}}\left[\operatorname{div}(\eta_0 \mathbf{u}_p) + \frac{1}{c_0^2}\frac{\partial \pi_H}{\partial t} - \frac{\partial \eta_0 u_p}{\partial x}\right]\end{aligned} \tag{197}$$

$$\begin{aligned}\frac{\partial \hat{u}_d}{\partial t} + \frac{\partial \hat{\pi}_H}{\partial x} &= \hat{R}_u \\ &= -\sqrt{\frac{\eta_0 \rho_0}{\xi}}\left\{(\mathbf{A}_d \mathbf{u})_x + \frac{1}{\rho}\frac{\partial \pi_I}{\partial x} + \left(\frac{1}{\rho} - \frac{1}{\rho_0}\right)\frac{\partial \pi_H}{\partial x} + \frac{1}{\rho}\frac{\partial \delta}{\partial x} + \frac{\partial}{\partial x}\left(\frac{|\mathbf{u}_p + \mathbf{u}_h|^2}{2}\right) - \frac{\partial u_p}{\partial t}\right\}\end{aligned} \tag{198}$$

Let λ^k and r^k, $k = 1 \ldots N$, be the eigenvalues and eigenvectors of the discretized operator $\hat{\mathscr{L}}_z$. $\hat{\pi}_H$ and $\hat{u}$ can be decomposed on the orthonormal basis formed by the eigenvectors r^k

$$\hat{\pi}_H(x,z,t) = \sum\nolimits_{k=1}^{N} \hat{\pi}_H^k(x,t) r^k(z) \tag{199}$$

$$\hat{u}_d(x,z,t) = \sum\nolimits_{k=1}^{N} \hat{u}_d^k(x,t) r^k(z) \tag{200}$$

with

$$\hat{\pi}_H^k(x,t) = \int_0^{L_{\text{top}}} \hat{\pi}_H(x,z,t) r^k(z)\mathrm{d}z \tag{201}$$

$$\hat{u}_d^k(x,t) = \int_0^{L_{\text{top}}} \hat{u}_d(x,z,t) r^k(z)\mathrm{d}z \tag{202}$$

System (197), (198) can then be rewritten after projection on the eigenvector r^k,

$$\lambda^k \frac{\partial \hat{\pi}_H^k}{\partial t} + \frac{\partial \hat{u}_d^k}{\partial x} = \hat{R}_{\pi_H}^k \tag{203}$$

$$\frac{\partial \hat{u}_d^k}{\partial t} + \frac{\partial \hat{\pi}_H^k}{\partial x} = \hat{R}_u^k \tag{204}$$

The system of Eqs. (203) and (204) is hyperbolic with wave speed $c_{\text{gw}}^k = \frac{1}{\sqrt{\lambda^k}}$. The wave speed c_{gw}^k is the speed of the gravity waves on the kth mode and the fastest gravity wave with speed c_{gw} is constraining the time step.

References

[1] A. Almgren, J. Bell, P. Colella, T. Marthaler, A Cartesian grid projection method for the incompressible Euler equations in complex geometries, SIAM J. Sci. Comput. 18 (5) (1997).

[2] F. Baer, J.J. Tribbia, On complete filtering of gravity modes through nonlinear initialization, Monthly Weather Rev. 105 (1977) 1536–1539.
[3] J. Bell, P. Colella, M. Welcome, Conservative front-tracking for inviscid compressible flow, in: Proc. 10th AIAA Computational Fluid Dynamics Conference, Honolulu, HI, pp. 814–822, 1991.
[4] L. Bonaventura, A semi-implicit semi-Lagrangian scheme using the height coordinate for a nonhydrostatic and fully elastic model of atmospheric flows, J. Comput. Phys. 158 (2000) 186–213.
[5] P. Bannon, On the anelastic approximation for a compressible atmosphere, J. Atmos. Sci. 53 (23) (1996) 3618–3628.
[6] I. Chern, P. Colella, A conservative front-tracking method for hyperbolic conservation laws, UCRL-97200 LLNL, 1987.
[7] T. Clark, A small-scale dynamic model using a Terrain-following coordinate transformation, J. Comput. Phys. 24 (1977) 187–214.
[8] P. Colella, D. Graves, B. Keen, D. Modiano, A Cartesian grid embedded boundary method for hyperbolic conservation laws, J. Comput. Phys. 211 (2006) 347–366.
[9] P. Colella, K. Pao, A projection method for low speed flows, J. Comput. Phys. 149 (2) (1999) 245–269.
[10] D. Durran, Another look at downslope windstorms. Part I: The development of analogs to supercritical flow in an infinitely deep, continuously stratified fluid, J. Atmos. Sci. 43 (21) (1986) 2527–2543.
[11] D. Durran, Improving the anelastic approximation, J. Atmos. Sci. 46 (11) (1989) 1453–1461.
[12] D. Durran, Atmospheric processes over complex Terrain, Meteorol. Monographs 23 (45) (1990) 59–81.
[13] D. Durran, J.B. Klemp, A compressible model for the simulation of moist mountain waves, Monthly Weather Rev. 111 (1983) 2341–2360.
[14] C. Gatti-Bono, P. Colella, A filtering method for gravitationally stratified flows, LBNL-57161.
[15] J. Holton, An Introduction to Dynamic Meteorology, third ed., Academic press, New York, 1992.
[16] C.-Y. Huang, A forward-in-time anelastic nonhydrostatic model in a terrain following coordinates, Monthly Weather Rev. 128 (2000) 2108–2134.
[17] H. Johansen, P. Colella, A Cartesian grid embedded boundary method for Poisson's equation on irregular domains, J. Comput. Phys. 147 (1) (1998) 60–85.
[18] T. Kato, K. Saito, Hydrostatic and non-hydrostatic simulations of moist convection: applicability of the hydrostatic approximation to a high-resolution model, J. Meteorol. Soc. Jpn. 73 (1) (1995) 59–77.
[19] R. Klein, Asymptotic analyses for atmospheric flows and the construction of asymptotically adaptive numerical methods, ZAMM 80 (2000) 765–777.
[20] Klemp, D. Lilly, Numerical simulation of hydrostatic mountain waves, J. Atmos. Sci. 35 (1978) 78–107.
[21] E.B. Kluzek, J. Olson, J.M. Rosinski, J.E. Truesdale, M. Vertenstein, User Guide to NCAR CCM3.6, Climate and Global Dynamics Division, National Center for Atmospheric Research, Boulder, CO.
[22] T. Keller, Implications of the hydrostatic assumption on atmospheric gravity waves, J. Atmos. Sci. 51 (13) (1994) 1915–1929.
[23] Y.-J. Kim, A. Arakawa, Improvement of orographic gravity waves parametrization using a mesoscale gravity wave model, J. Atmos. Sci. 52 (11) (1995) 1875–1902.
[24] D. Lilly, A comparison of incompressible, anelastic and Boussinesq dynamics, Atmos. Res. 40 (1996) 143–151.
[25] P. McCorquodale, P. Colella, H. Johansen, A Cartesian grid embedded boundary method for the heat equation on irregular domains, J. Comput. Phys. 173 (2001) 620–635.
[26] M. Minion, Semi-implicit spectral deferred correction methods for ordinary differential equations, Commun. Math. Sci. 1 (3) (2003) 471–500.
[27] J. Oliger, A. Sundstrom, Theoretical and practical aspects of some initial boundary-value problems in fluid dynamics, SIAM J. Appl. Math. 35 (1978) 419–446.
[28] W. Peltier, T. Clark, The evolution and stability of finite-amplitude mountain waves. Part II: Surface wave drag and severe downslope windstorms, J. Atmos. Sci. 36 (1979) 1498–1529.
[29] R. Pember, J. Bell, P. Colella, W. Crutchfield, M. Welcome, An adaptive Cartesian grid method for unsteady compressible flow in irregular regions, J. Comput. Phys. 120 (2) (1995) 278–304.
[30] D. Randall, The anelastic and Boussinesq approximations, unpublished, 2000. Available from: <http://kiwi.atmos.colostate.edu:16080/group/dave/drweb/AneBous.pdf>.
[31] G. Rosatti, D. Cesari, L. Bonaventura, Semi-implicit, semi-Lagrangian modelling for environmental problems on staggered Cartesian grids with cut cells, J. Comput. Phys. 204 (2004) 353–377.
[32] K. Saito, A numerical study of the local downslope wind "Yamaji-kaze" in Japan – Part 3: Numerical simulation of the 27 September 1991 windstorm with a non-hydrostatic multi-nested model, J. Meteorol. Soc. Jpn. 72 (2) (1994) 301–328.
[33] C. Temperton, D.L. Williamson, Normal mode initialization for a multilevel grid-point model. Part I: Linear aspects, Monthly Weather Rev. 109 (1981) 729–743.
[34] J.J. Tribbia, A simple scheme for high-order nonlinear normal mode initialization, Monthly Weather Rev. 112 (1984) 278–284.
[35] D.L. Williamson, C. Temperton, Normal mode initialization for a multilevel grid-point model. Part I: Nonlinear aspects, Monthly Weather Rev. 109 (1981) 744–7757.